Short-term internship report

ISOLDE Solid-state physics group, CERN
BSc General Engineering, DTU

Local temperature dependence study of bismuth ferrite upon ^{111}In implantation: an atomic point of view for the In-site occupation

Author
Andrea González Boa

CERN ID/ DTU ID
164504 / s174370

Supervisors (CERN)
Dr. Juliana Schell
Dr. Gerda Neyens

Department
ISOLDE Solid-state physics
ISOLDE physics

Supervisors (DTU)
Prof. Hugh Simons
Prof. Cathrine Frandsen

DTU Physics
DTU Physics

Abstract

Multiferroic materials have gained a lot of attention in the past half century for their potential application in the technology industry, as they can be used in data storage, spintronics, and microelectronic devices.[1] This group of materials often show a low Néel and Curie temperature, usually below room temperature, leading to the loss of their multiferroic properties. That is why bismuth ferrite ($BiFeO_3$ or BFO) has gained a lot of attention within multiferroic materials, as both of these temperatures are well above room temperature, and thus showing multiferroic properties that can be exploited for the development of technologies.

This work presents the study of the temperature dependence of the nuclear quadrupole interactions in bismuth ferrite with time-differential $\gamma - \gamma$ perturbed angular correlation (TDPAC) spectroscopy using ^{111}In(^{111}Cd) as a probe nuclei. The site assignment for the probe is discussed and it is most probable that the lattice location for the presented measurement conditions is the Fe-site. The x-ray powder diffraction (XRD) technique was employed to investigate the macroscopic crystal structure before and after the TDPAC experiments and thus investigate how the thermal treatment during the TDPAC measurements affected the sample. XRD provided with the amount of secondary phase present in the samples, and this varies according to the thermal treatment carried out.

This work further presents the data taken below the Néel temperature. However, the fitting of combined hyperfine interactions is very complex and this analysis is foreseen as a future step.

Moreover, a comparison was made using data obtained with the nuclear probe ^{111m}Cd(^{111}Cd) to study the differences in the location of the probe within the BFO structure, as well as a comparison with other studies in which BFO is doped with indium.

The results with BFO(^{111}In) showed that a single electric field gradient was observed in all temperatures during the TDPAC experiments. The observable frequency associated with the α phase follows a parabolic trend with offset, throughout the values 128-98 [Mrad/s], with very small values of asymmetry parameter ($\eta \approx 0$) and damping ($\delta \approx 0$). The change to the β phase was observed with the drop in the frequency values to ~ 20 [Mrad/s], as well as with the increase of the asymmetry parameter towards 1 and the damping, reaching values of 10-12%. This indicates a first order transition. By comparing the obtained results with ab initio calculations of the electric field gradient and asymmetry parameter from the previous BFO(^{111}Cd) research, which is possible because both probe atoms share intermediate state, it was possible to assign the ^{111}In probe to the substitutional Fe-site.

Acknowledgements

This work is the result of the hard work of the many people involved, and I would like to take this opportunity to acknowledge their efforts. Without their scientific contribution, this work would have not been possible.

I would like to thank my CERN supervisor *Dr. Juliana Schell*, ISOLDE Solid-state Physics coordinator, for the opportunity to be part of this work as well as for her trust and guidance. Without her constant input and dedication, this work would not have reached so far. I would also like to thank the ISOLDE Physics group leader, *Dr. Gerda Neyens*, and coordinator, *Dr. Karl Johnston*, for the opportunity to work at ISOLDE physics.

From DTU, I would like to thank my supervisor *Prof. Hugh Simons*, associate professor at DTU Physics, and my co-supervisor, *Prof. Cathrine Frandsen*, professor at DTU Physics. Without them, I would not have been granted the opportunity to do this traineeship. I would also like to mention *Luise Theil Kuhn*, head of the BSc General Engineering, and thank her for her constant support, without which I would have never had the motivation to reach working at CERN.

I have to deeply thank *Georg Marschick*, from Vienna University of Technology, without who's work the kick-off of this work would have been much harder.

I would like to personally thank *Prof. Doru C. Lupascu*, from the Institute for Materials Science and Center for Nanointegration Duisburg-Essen (CENIDE), University of Duisburg-Essen, for his guidance and support in the bi-weekly meetings. Also from the University of Duisburg-Essen, I would like to mention and thank *Astita Dubey* and *Merlin Schmuck* for the XRD measurements, *Dr. Marianela Escobar*, for the sample preparation and *Vladimir Shvartsman* for the fruitful discussions. A special thank you goes to *Thien Thanh Dang*, from this same team, for his willingness to always assist us during this work.

From the Helmholtz-Institut für Strahlen- und Kernphysik, University of Bonn, I would like to thank *Ms. Cornelia Noll, Dr. Marius Arenz* and *Prof. Beck* for the high quality ion implantation.

I would also like to acknowledge *Dr. Dmitry Zyabkin*, Technische Universität Ilmenau, and *Dr. Konstantin Glukhov*, Uzhgorod National University, for their collaboration during the TDPAC measurements. Their long hours in the lab has made this work possible.

I would like to thank *João Nuno Santos Gonçalves*, CICECO - Aveiro Institute of Materials and Departamento de Física, University of Aveiro, for his efforts in performing DFT simulations to back up our experimental results.

I would also like to acknowledge the financial support received from the Federal Ministry of Education and Research (BMBF) through grants 05K16PGA, and 05K16SI1 and the support from the ISOLDE collaboration, as well as the support of the European Union's Horizon 2020 Framework research and innovation program under grant agreement no. 654002 (ENSAR2) given to the ISOLDE experiment IS647.

To my family and friends, to whom I owe it all.

Contents

Chapter 1

Introduction and background

During the last century, multiferroic materials have gained a lot of attention mainly for their potential application in the technology industry, as they can be used in data storage, spintronics, and microelectronic devices.[1] Within the group of materials that exhibit these characteristics, there is a larger focus on the research of $BiFeO_3$ (also known as BFO) as its Néel temperature and Curie temperature are well above room temperature ($T_N \approx 370°C$ and $T_C \approx 822°$C).[2] As a result, BFO shows antiferromagnetic and ferroelectric properties at room temperature and thus it could be implemented for the development of future technologies such as sensors, memory devices, spintronics, and photovoltonics.[1]

1.1 Multiferroic materials

Multiferroics are defined as materials that exhibit more than one of the primary ferroic properties in the same phase.[3] These forms refer to:

- Ferromagnetism: magnetisation that is switchable by using an applied magnetic field. For this paper, this property includes every kind of magnetic appearance with a macroscopic magnetic moment M plus antiferromagnetism.
- Ferroelectricity: electric polarization that can be switched by an applied electric field.
- Ferroelasticity: deformation that is switchable by an applied stress.

There is a big focus on materials in which a combination of ferromagnetic and ferroelectric properties can be shown, due to the fact that when these forms appear simultaneously[4], and therefore new ways of exploiting material properties like electrically controlled magnetization, and vice versa, are possible. These materials are known as magnetoelectric (ME) multiferroics.[3]

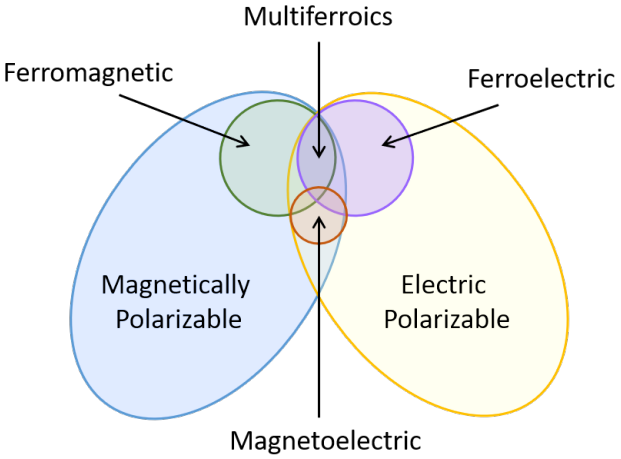

Figure 1.1: Schematic figure showing the relationship between multiferroic materials and the magnetoelectric effect.

1.1.1 Magnetoelectric (ME) multiferroics

When the properties of ferromagnetism and ferroelectricity are combined in a material such that the magnetic properties can be controlled with an electric polarization and vice versa, it is known as the magnetoelectric effect. When this coupling is found intrinsically in a material, such material is known as magnetoelectric (ME)[5].

Single phase ME multiferroics show the ME effect intrinsically by the magnetoelectric susceptibility α, which describes the linear response of the electric polarization to a magnetic field, and vice versa. From the free energy of a crystal this linear ME coupling constant can be derived[6]:

$$F(\vec{E},\vec{H}) = F_0 - P_i^s E_i - M_i^s H_i - \frac{1}{2}\epsilon_0\epsilon_{ij}E_iE_j - \frac{1}{2}\mu_0\mu_{ij}H_iH_j - \alpha_{ij}E_iH_j - \dots \tag{1.1}$$

where F denotes the free energy, $\vec{E},\vec{H}$ the electric and magnetic field strength, respectively, P^s, M^s the spontaneous electric polarization and magnetisation, respectively, and ϵ and μ are the electric and magnetic susceptibility. To find the electric polarization, the first derivative of E of equation 1.1 is calculated:

$$P_i(\vec{E},\vec{H}) = -\frac{\delta F}{\delta E_i} = P_i^s + \epsilon_0\epsilon_{ij}E_j + \alpha_{ij}^{EM}H_j + \dots \tag{1.2}$$

And for the magnetization, the same procedure is followed for M:

$$M_i(\vec{E},\vec{H}) = -\frac{\delta F}{\delta H_i} = M_i^s + \mu_0\mu_{ij}H_j + \alpha_{ij}^{ME}E_i + \dots \tag{1.3}$$

From these two equations, 1.2 and 1.3, it can be seen that the magnetoelectic susceptibility affects the electric polarization by terms of the magnetic field strength H (term $\alpha_{ij}^{EM}H_j$), and the magnetisation by the electirc field strength E (term $\alpha_{ij}^{ME}E_i$). The magnetoelectric susceptibility in both of these terms is symmetrical, and thus the effect has the same strength in both properties. The following terms of equation 1.1 have not been further mentioned because of their very small contribution to the effect.

The possibility of combining the magnetic and electric properties of materials this way opens up many possibilities in for material design. Nowadays these materials are being studied in depth for future applications in the spintronic industry, in sensoric devices, microwave devices and ME memories[1]. For this implementation, an important quality is that the material show the ME properties at room temperature, and there are very few that does, that is why the study of bismuth ferrite ($BiFeO_3$ or BFO) has such a great attention nowadays as BFO is part of this small group of materials.

1.2 Perovskite structure

The perovskite structure is named after the calcium titanium oxide mineral perovskite $CaTiO_3$. Perovskites are a group of materials with general chemical formula ABX_3, where A and B are two different cations, usually also of different sizes, and X is an anion (normally oxygen) which bonds to the cations.[7] The cations A and B are coordinated by corner linked octahedra of the X anions, and the B cation sits in the center of these octahedra, forming a three dimensional network. The A cation is placed in the resulting cuboctahedral gaps, and as a consequence, there is a 12-fold X coordination. However, this definition is only valid for the ideal, not distorted perovskite structure, the aristotype with point group $Pm\bar{3}m$[6]. Different cation sizes produce distortions and tilting of the octahedra, leading to changes in coordination and morphology of the polyhedra. These changes are very important to describe the electric and magnetic properties of the compounds.

The Goldschmidt tolerance factor describes the magnitude of the distortion, and it is defined as:

$$t = \frac{r_A + r_X}{\sqrt{2}\,(r_B + r_X)} \tag{1.4}$$

Here, r_A, r_B and r_X refer to ionic radii of the involved A and B cations, and the X anion. The ideal perovskite structure mentioned above, of the space group $Pm\bar{3}m$, shows a tolerance factor of $t = 1$. It is said that a perovskite is distorted when $0.8 < t < 0.89$. From the $Pm\bar{3}m$ space group symmetry, group-subgroup relationships are derived. The space group of the BFO α-phase is defined as $R3c$ and for the β-phase, $Pbnm$, which are not directly related between group and subgroup, and this means that the phase transition from α-BFO and β-BFO is of first order. Once the results are presented, this will be better understood.

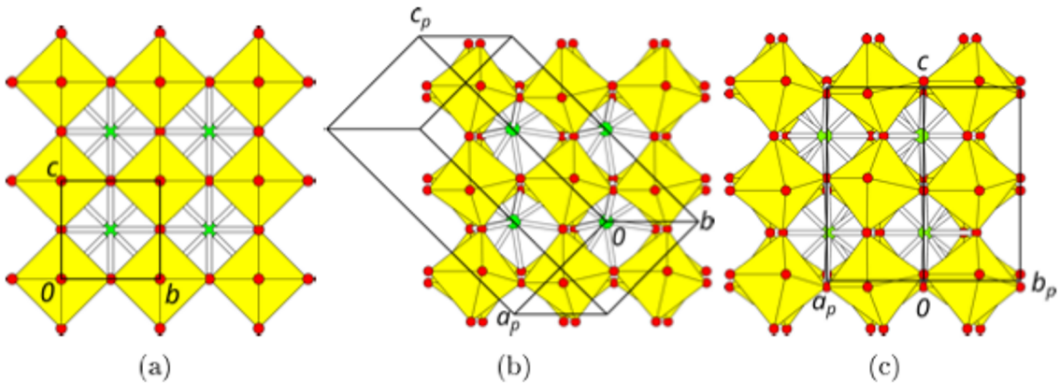

Figure 1.2: (a) The $Pm\bar{3}m$ ideal structure viewed down [100]. (b) Distorted α-BFO $R3c$ perovskite structure hexagonal unit cell viewed down [42$\bar{1}$], (c) Distorted β-BFO $Pbnm$ perovskite structure orthorhombic unit cell viewed down [110]. Taken from literature.[6]

Chapter 2

Bismuth ferrite

As mentioned previously, bismuth ferrite, also referred to as $BiFeO_3$ or BFO, is a material that drags a lot of attention in nowadays research due to its antiferromagnetic and ferroelectric properties, which are shown at room temperature.

It is commonly synthesized through sintering stoichiometric mixtures of Bi_2O_3 and Fe_2O_3.

2.1 BFO crystal structure

Despite the extensive research around it, there is still not an agreement about its crystal structure in the temperature range surrounding T_C, during the $\alpha - \beta$ phase transition. In the following section, the α and β phase of BFO are going to be analysed in greater detail.

2.1.1 α-phase

According to literature[1],[2],[8] there is an agreement with respect to the crystal structure of BFO in the α-phase, which shows a rhombohedral $R\mathcal{3}c$ structure with the cell parameters $a = 5.58$Å and $c = 13.87$Å in the hexagonal settings at room temperature. The stability of this phase can be divided into two regions, separated by the Néel temperature ($T_N \approx 370$°C). Below such, including at room temperature, BFO shows antiferromagnetic (AFM) properties. Above T_N is there the paramagnetic (PM) region, shown until the Curie temperature ($T_C \approx 822$°C). Around this point, a ferroelectric-paraelectric phase transition appears into the β-phase which is followed by a sudden volume contraction. Before this ferroelectric transition, BFO is characterized by a very large spontaneous polarization ($P \approx 90 - 100\mu$C cm^{-2})[9],[10] in the pseudocubic [111] direction. This direction is also the axis of rotation of the octahedral tilting. The spontaneous polarization along the [111] axis modifies the $Pm3m$ space group (corresponding to an ideal cubic perovskite) to the rhombohedral $R3m$.

2.1.2 β-phase

In spite of the numerous research around BFO, the symmetry of the crystal structure of the β-phase was still subject of discussion. Figure 2.1 shows an overview of the discussions around the structure of this phase. Haumont et al.[11] (2006) suggests a $Pm\bar{3}m$ symmetry after performing Raman spectroscopy. Kornev et al.[12] (2007) suggest symmetry $I4/mcm$ after ab initio calculations; while Palai et al.[13] (2008), using Raman spectroscopy, Differential Thermal Analysis (DTA) and XRD, presents a $P2mm$ structure. Later on in 2008, again Haumont et al.[14] proposes $P21m$ symmetry, supported by XRD measurements. Selbach et al.[15] in 2008 presented a symmetry of $R3c$ for this phase in BFO. It was finally suggested that the β-phase shows a orthorhombic $Pbnm$ structure, based on the research by Arnold et al.[8] in 2008 with Powder Neutron Diffraction (PND), by Wei et al.[16] in 2019 and Marschick et al.[2] (2020), where TDPAC and XRD were performed. These groups suggest $Pbnm$ symmetry for the β-phase, with the cell parameters of $a = 5.61$Å and $c = 7.97$Å. Moreover, there is another phase transition occurring at even higher temperatures, in which the β-phase changes into a cubic γ-phase[1]. This is another argument that supports the disagreement with the suggested cubic structure of the β-phase[11].

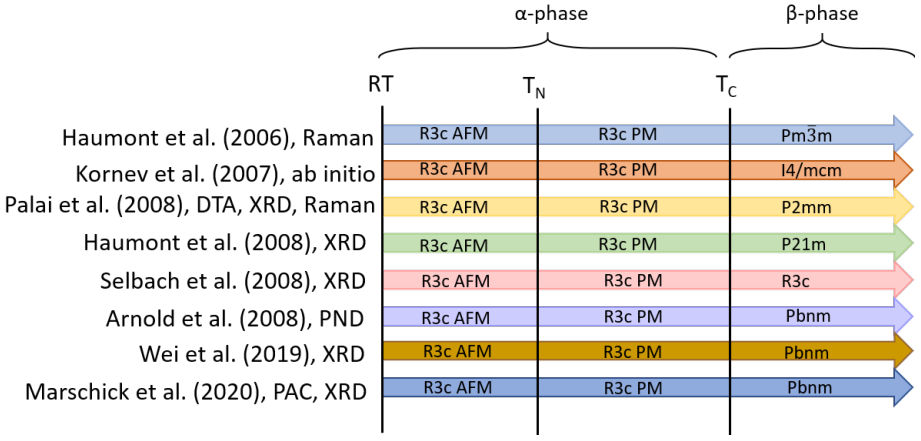

Figure 2.1: Figure summarizing the different research around the crystal structure of α and β phase of BFO. Based on literature G. Marschick et al. "Multiferroic bismuth ferrite: Perturbed angular correlation studies on its ferroic $\alpha - \beta$ phase transition". In: Phys. Rev. B 102, 224110 – Published 29 December 2020.

Figures 2.2a and 2.2b show stereoscopic images of the crystal structures of the α ($R3c$) and the β ($Pbnm$) phase of BFO, respectively. The bismuth atoms shown in purple, the iron atoms in golden and the oxygen atoms are shown in red.

One of the main reasons to the lack of standard agreement with respect to the crystal structure of the β-phase is that BFO decomposes at high temperatures, meaning that secondary phases occur. This makes it much harder to determine the structure at high temperatures. Arnold et al.[8] performed crystallographic analysis of the PND data by using the Rietveld method,

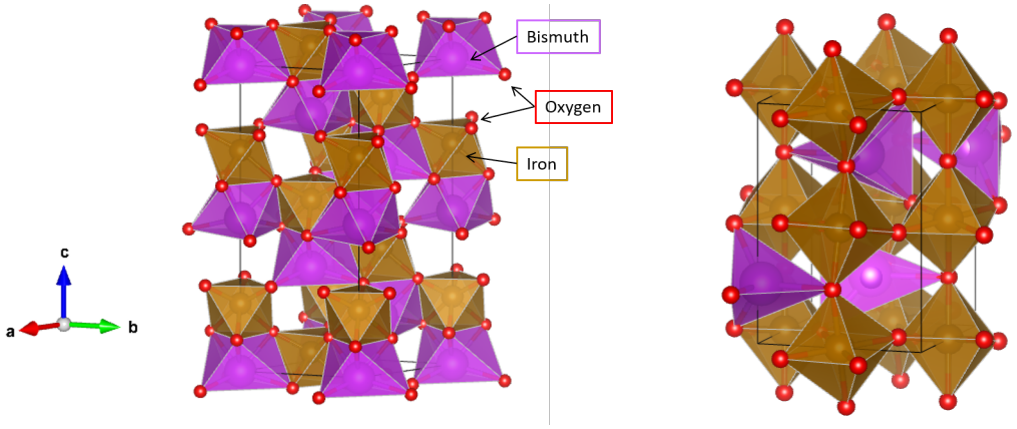

(a) *R3c*, α-phase. (b) *Pbnm*, β-phase.

Figure 2.2: BFO structure in the α-phase (left) and β-phase (right). Made with VESTA[17] using file of structural parameters obtained from Crystallographic Open Database (COD)[18],[19],[20],[21],[22],[23],[24].

and the results agree that at a temperature of 810-815°, the secondary phase $Bi_2Fe_4O_9$ starts appearing and it accounts for approximately 2.5% of the impurities observed. Suresh et al.[25] performed XRD studies where this problem is eradicated by doping BFO with Lanthanum, which stabilizes the material at higher temperatures avoiding the formation of unwanted secondary phases (such as $Bi_2Fe_4O_9$ or $Bi_{25}FeO_{40}$). Furthermore, it does not introduce changes of the low temperature crystal symmetry, nor does it change the Curie point of BFO, as opposed to doping with other rare earth materials or transition metals.

With respect to the magnetic properties of BFO, it seems that it shows a G-type antiferromagnet at room temperature, meaning that each magnetic moment is surrounded by six inter- and intraplanary opposed magnetic moments[6].

2.2 Ion bonds

As previously described, the Goldschmidt tolerance factor (Eq. 1.4) is one way of describing the distortion of a perovskite structure. When this ratio is smaller than one, as it occurs with BFO ($t = 0.88$, with Bi^{+3} in eightfold coordination and Fe^{+3} in sixfold coordination and high spin)[1], the oxygen octahedra must contort in order to fit into a cell that is too small. For BFO, rotation angle of the oxygen octahedra is approximately 11–14° around the polar [111] axis,[1],[9] with the directly related Fe–O–Fe angle, θ ca. 154–156°. The distortion along the [111] direction arises from the lone pair, where the s^2 electrons from the Bi hybridize with the oxygen's p electron to induce ferroelectricity.[9] Moreover, the Fe–O–Fe angle is important because it controls both the magnetic exchange and orbital overlap between Fe and O, and this determines the magnetic ordering temperature and the conductivity[1].

From Arnold et al.[8], it is proven that the bismuth site changes from a six-coordination site

with respect to oxygen in the *R3c* phase to an eight coordination in the *Pbnm* phase, whereas the iron-site does not change in coordination with oxygen. Nonetheless, the FeO_6 octahedra change drastically at T_C. During the *R3c* phase, the Fe-O bonds are characterized by three short degenerate and three long degenerate bond lengths. When the phase transition happens, these bond lengths become more equal in size, up to the point where in the *Pbnm* phase the octahedron is much more regular, with bond lengths much more equal but occurring as three degenerate pairs, as Fe is on an inversion center[8]. This implicates that three of these bonds become longer (from $\sim$ 1.95Å to $\sim$ 2.03Å), whereas the other three become shorter (from $\sim$ 2.12Å to $\sim$ 2.03Å). Refer to Figure 2.5 to see the evolution of the bond lengths. The repercussion this might have will be discussed later on.

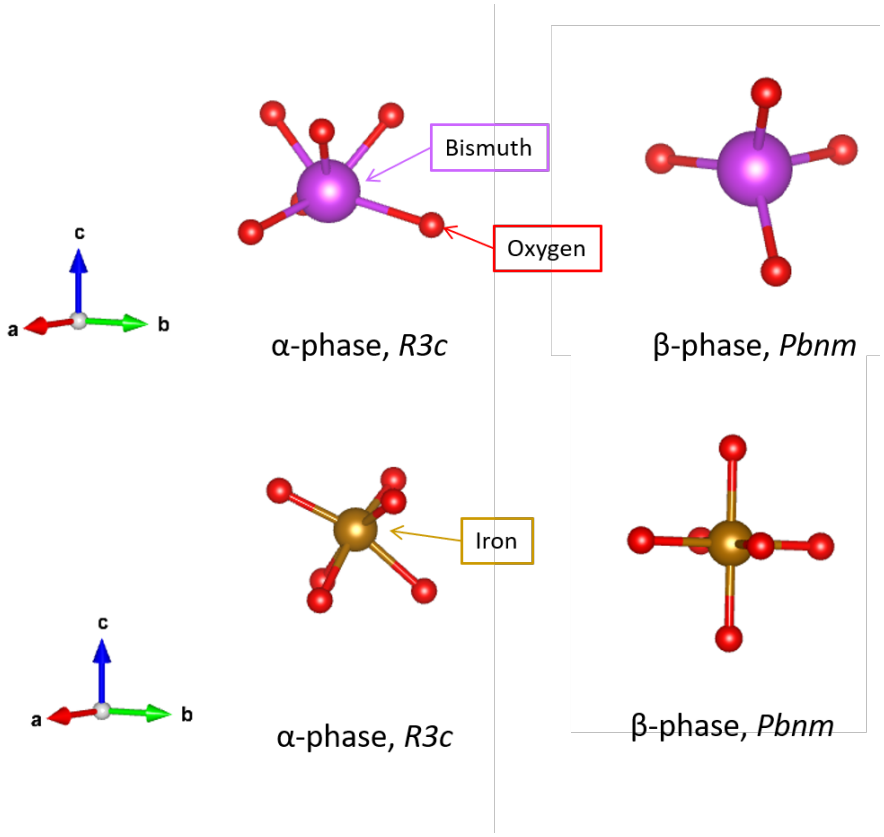

Figure 2.3: Change in coordination and ion bond lengths of Bi-O (top) and change in bond lengths of Fe-O (bottom) with phase transition from *R3c* to *Pbnm* symmetry. Made with VESTA[17].

These changes in coordination (Bi-O) and in bond lengths for Bi-O and Fe-O octahedra are shown in Figure 2.3.

Figure 2.4.a shows the oxygen octahedral angle (denoted as ω) dependency on temperature across the phase transition from the α to the β phase in BFO. This confirms the changes in

lattice parameters as well as in the unit cell volume, as it can be seen that the angle narrows down with increasing temperature[8].

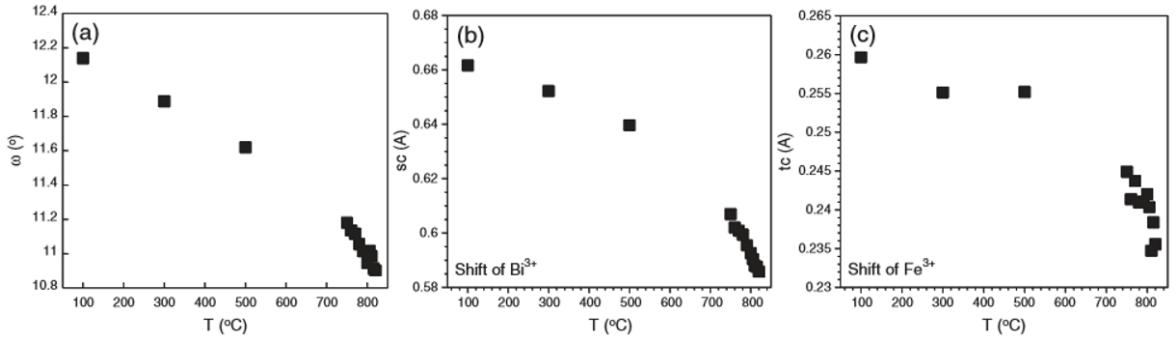

Figure 2.4: Thermal evolution of the *R3c* α-phase (a) Oxygen octahedral rotation angle, ω, (b) polar shift of Bi^{3+} ion from its ideal perovskite position, *sc*, and (c) polar shift of Fe^{3+} ion from its ideal perovskite position, *tc*. Error bars are smaller than the symbols. Reprinted figure with permission from Donna C. Arnold et al. "Ferroelectric-paraelectric transition in $BiFeO_3$: crystal structure of the orthorhombic β phase". In: Physical Review Letters 102.2(2009), p. 027602. Copyright (2021) by the American Physical Society.

Figure 2.5.a shows the normalized unit cell volume per $BiFeO_3$ unit as a function of temperature, which shows an abrupt decrease at the $\alpha - \beta$ transition. Figures 2.5.b and 2.5.c show the evolution of Fe-O bond lengths, reflecting the loss of the polar displacement of Fe^{3+} within its octahedron at T_C. Figures 2.5.d and 2.5.e show the evolution of the Bi-O environment showing the change from a six-coordinate site in the *R*3*c* phase (closed squares) to an eight-coordinate site in the *Pbnm* phase (open squares). In all plots, error bars are smaller than the symbols.

It is important to add that the crystal structure of BFO offers two different sites for the implanted ^{111}In probe, namely the A-site, substituting the bismuth atoms and the B-site, substituting iron. Thus, it is important to understand how the ion bonds in BFO change with the phase transition in order to understand the results obtained, which will depend on the location of the probe within the BFO structure.

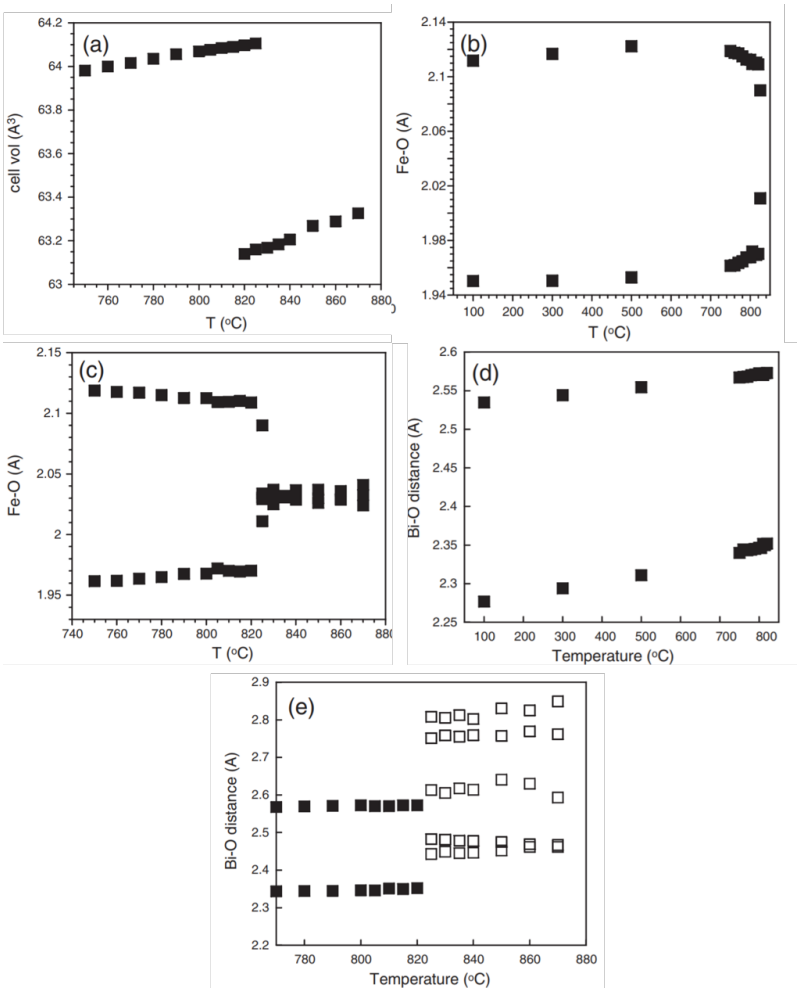

Figure 2.5: Graphs showing the (a) Normalized unit cell volume per BFO unit, (b) and (c) evolution of Fe-O bond lengths and (d) and (e) evolution of Bi-O bond lengths. Reprinted figure with permission from Donna C. Arnold et al. "Ferroelectric-paraelectric transition in $BiFeO_3$: crystal structure of the orthorhombic β phase". In: Physical Review Letters 102.2(2009), p. 027602. Copyright (2021) by the American Physical Society.

Chapter 3

^{111}In Probe

The TDPAC technique depends on the proper incorporation of a nuclear probe in a material, so that the hyperfine interactions between this probe and the neighbour atoms can be studied. In this case, the studied material is bulk BFO, and the chosen probe is the radioactive isotope ^{111}In.

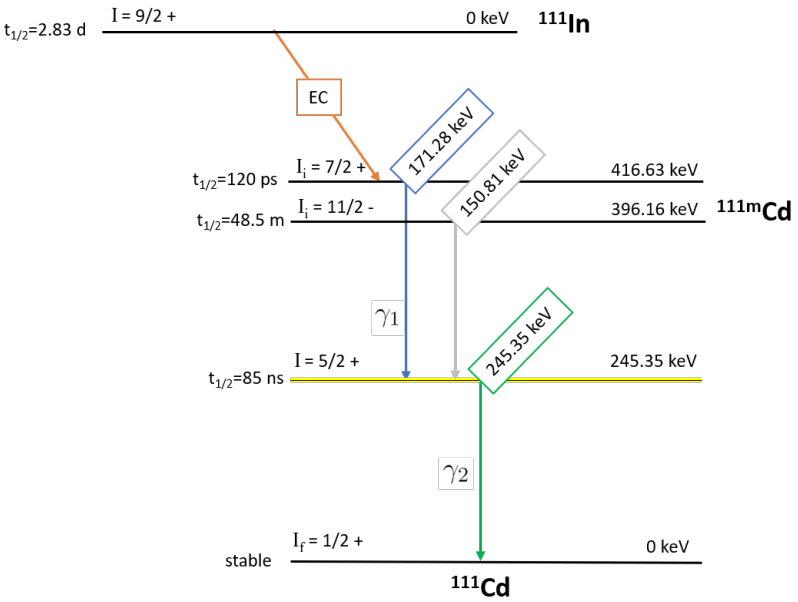

Figure 3.1: Decay scheme of ^{111}In and ^{111m}Cd.

Figure 3.1 shows the decay scheme of ^{111}In and it was based on the figure available in the software NUCLEI[26]. Here it can be seen that the chosen isotope ^{111}In decays to ^{111}Cd through an excited state of Cd, reaching the later by electron capture (EC), whilst the probe

^{111m}Cd decays to ^{111}Cd directly by an isomerical transition (IT). The fact that both probes ^{111}In(^{111}Cd) and ^{111m}Cd(^{111}Cd) present the same intermediate state allows us to compare the results obtained in this research with a previous research made also by the team of ISOLDE solid-state physics group at CERN, in which they study BFO after ^{111m}Cd implantation.[2]

	^{111}**In**	^{111m}**Cd**
Implantation depth (SRIM)	216 Å	116 Å
Valence	3+	2+
Intermediate state	±5/2	±5/2
Half life ($\tau_{1/2}$)	2.83 days	48.54 min
γ-rays energy	γ_1 = 171.28 keV γ_2 = 245.35 keV	γ_1 = 150.81 keV γ_2 = 245.35 keV
Decay type	EC	IT
Theoretical A_{22} values[26]	-0.1782	0.1782
Probe isotope	^{111}Cd	^{111}Cd
Probe location	B-site	A-site

Table 3.1: Parameters to compare the different probe.[27]

From Table 3.1 it can be seen the different factors taken into account to make a complete comparison between the probe ^{111}In and ^{111m}Cd. The implantation depth was computed with the software SRIM[28], using the option of TRansport of Ions in Matter (TRIM) calculation. For the probe ^{111}In, the values to input are such as an accelerator voltage of 80keV and an implantation angle of 10°; whereas for ^{111m}Cd, these parameters were set to 30keV and 0°, respectively. Another parameter to input was the density of BFO, which was set to 8.4 g/cm^3. The ion implantation depth was then computed to 216Å for ^{111}In and 116Å for ^{111m}Cd.

Furthermore, the chemistry of both probes also varies as they come from different parents isotopes, and this could make a big difference in the location of the probe within the BFO structure. In the previous research, it has already been concluded that ^{111m}Cd is located in the A-site, corresponding to the substitution of Bi atoms in BFO. Later on, it will be discussed which site occupies ^{111}In.

Something that plays in our favor, and that can also be seen from Table 3.1, is that the half life of the probe ^{111}In is of 2.83 days, making it possible to take many TDPAC temperature measures using the sample, something that is not possible with the short half life of 48.54 min of the probe ^{111m}Cd.

CN	Ion				
	Cd^{2+}	Bi^{3+}	Fe^{3+}	In^{3+}	Mn^{3+}
IV	0.84	-	0.49	-	-
V	0.87	0.99	-	-	0.58
VI	0.95	1.02	0.55 (LS) 0.645 (HS)	0.79	0.58 (LS) 0.65 (HS)
VII	1	-	-		
VIII	1.07	1.11	-	0.923	-
XII	1.31	-	-		

Table 3.2: Ionic radii of different elements relevant for this research.

This probe was chosen due to its similar ionic radius to iron in the VI coordination configuration. Different researches have studied the substitution of In in the A-site of BFO, and thus replacing bismuth atoms. When doping BFO with In, the substitution in the A-site is aimed due to the smaller ionic radius of the isotope, as it is believed to improve the multiferroic properties of BFO by the cation size effect[29]. Other research that co-dopes BFO nanoparticles with In and Mn seems to assign In to the A-site and Mn to the B-site also due to their ionic radii closer to Bi and Fe, respectively[30], in order to improve the multiferroic properties of the material. Nonetheless, that does not seem to be the case here. In^{+3} in the VI coordination number presents an ionic radius much closer to the ionic radius of Fe^{+3} than of Bi^{+3}, for what it is considered that In will be located in the B-site of BFO for this work.

However, to the best of our knowledge, there is just one research that take into account the substitution of In in the B-site, the Fe-site[31] (more information later on, in section 8.3).

Chapter 4

Time-Differential Perturbed Angular Correlation (TDPAC)

The perturbed angular correlation (TDPAC) spectroscopy is used to study the local crystal lattice environment. The technique involves studying the angular correlation between two γ-rays emitted in the decay cascade from a decaying radioactive probe, which is previously incorporated in the material. When the first γ-ray is emitted, the nuclear probe decays to the intermediate state. The emission of a second γ-ray takes the probe to its final decay state, also called ground state. It is based on the hyperfine interactions which occur when the nuclear moments of the probe atoms interacts with its electromagnetic lattice environment fields. This leads to an inhomogeneous population of the m-states in the intermediate state. The following anisotropy of the γ emission gives information on the local structure of the probed sample. As TDPAC is a tracer technique, very few probe atoms are required and therefore, the overall chemistry structure of the material is not affected.

Here, the basic principles of the TDPAC formalism are shown for static quadrupole interactions. Additional information regarding the TDPAC technique and its formalism can be found in the literature[32],[33],[34].

4.1 The Electric Field Gradient (EFG)

An electric field gradient (EFG) is caused by charge distributions around the probe atom and is associated to a nuclear quadrupole interaction. This parameter is defined as the second spacial derivative of the electrostatic potential. By the diagonalization of the interaction Hamiltonian, plus rotating the tensor into its principal component coordinate system and the use of the Laplace equation (see Appendix B for detailed calculation), the EFG can be described by its largest component V_{zz} and the asymmetry parameter, η:

$$\eta = \frac{V_{xx} - V_{yy}}{V_{zz}} \tag{4.1}$$

The asymmetry parameter have values between 0 (axial symmetric) and 1 (asymmetric).

Moreover, V_{zz} is also used to describe the quadrupole interaction frequency, ω_q:

$$\omega_q = \frac{eQV_{zz}}{4I(2I-1)\hbar} \tag{4.2}$$

where e is the electron charge, Q the quadrupole moment of the intermediate state of the probe nucleus, I its angular momentum and $\hbar$ the reduced Planck's constant. With a symmetric EFG ($\eta = 0$), the lowest detectable substate-transition frequency is defined as $\omega_0 = k\omega_q$. The parameter k equals to 6 for the half-integer values of spin momentum, as it happens with the chosen probe ^{111}In with $I = 5/2$. The transition frequencies can then be described as $\omega_1 = 6\omega_Q, \omega_2 = 12\omega_Q$ and $\omega_3 = \omega_1 + \omega_2$, following a ratio of $1 : 2 : 3$. This ratio can be easily observed in Figure 4.1. If $\eta \neq 0$, the sublevel energies depend on η and generally can not be solved analytically.

The transition frequencies are defined as $\omega_n = n\omega_0$, and they are function of ω_q and η when the latter is non-equal to 0:

$$\omega_1 = 2\sqrt{3}\alpha\omega_q \sin\left(\frac{1}{3}\arccos(\beta)\right) \tag{4.3}$$

$$\omega_2 = 2\sqrt{3}\alpha\omega_q \sin\left(\frac{1}{3}(\pi - \arccos(\beta))\right) \tag{4.4}$$

$$\omega_3 = 2\sqrt{3}\alpha\omega_q \sin\left(\frac{1}{3}(\pi + \arccos(\beta))\right) \tag{4.5}$$

with

$$\begin{aligned} \alpha &= \sqrt{\frac{28\,(3+\eta^2)}{3}} \\ \beta &= \frac{80\,(1-\eta^2)}{\alpha^3} \end{aligned} \tag{4.6}$$

These transition frequencies define the transitions between substates levels created by a hyperfine splitting of the intermediate state. This can be observed in Figure 4.1.

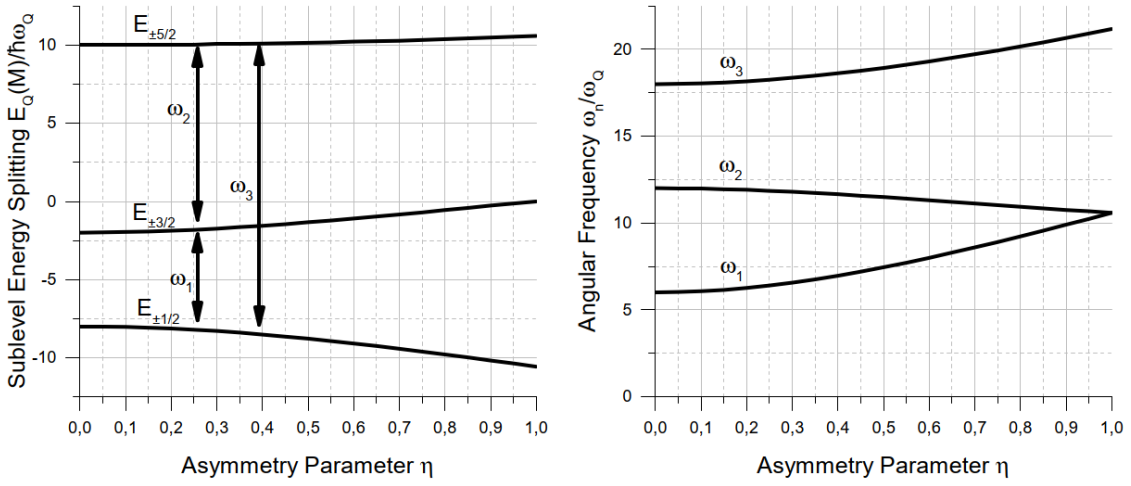

Figure 4.1: Change of sublevel energies $E_Q(M)$ with increasing asymmetry parameter (η) and resulting change of angular frequencies ω_n. Reference value of $\omega_Q = 10$ Mrad/s, valid only for $I = 5/2$. Taken from literature G. Marschick et al. "Multiferroic bismuth ferrite: Perturbed angular correlation studies on its ferroic $\alpha - \beta$ phase transition". In: Phys. Rev. B 102, 224110 – Published 29 December 2020.

4.2 TDPAC methodology

The TDPAC technique relies on the γ-γ cascade decay that occurs when the excited probe nucleus decays to the ground state, through the intermediate state, as shown in Figure 4.2. An angular correlation is then measured from the first γ-ray to the second, which differ in energy and detection time, and the hyperfine interactions between the probe nucleus and the neighbour atoms can be detected. Since the spin of the probe nuclei are randomly oriented in space, the γ emissions from the sample are isotropic. To make the pattern anisotropic, a preferential direction is chosen as the direction where γ_1 is detected. A certain spin orientation is selected and all nuclei with this spin orientation contribute to the detected signal. This way, by defining an axis in the direction γ_1, γ_2 is detected anisotropically with respect to the former.

The probability to detect the second γ ray with respect to the first is described by the angular correlation function:

$$W(\theta) = \sum_{k=0}^{k_{max}} A_{kk} P_k(\cos\theta) \tag{4.7}$$

where k only has even values (due to the conservation of parity), θ is the angle between the γ rays and A_{kk} measures the deviation of the angular correlation from the isotropic distribution, known as the anisotropy coefficient (more about this in section 4.4). The theoretical values of this coefficient are taken from literature[26]. The values of k obey: $0 \leq k \leq$ minimum of $(2I, L_1 + L_1', L_2 + L_2')$, and $P_k(\cos\theta)$ refers to the Legendre polynomial. Equation 4.7

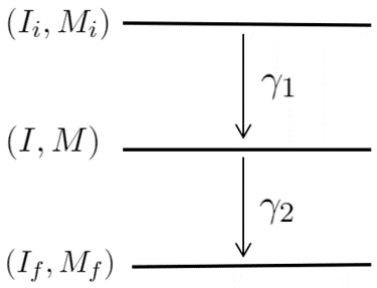

Figure 4.2: $\gamma - \gamma$ decay scheme from excited state (I_i, M_i) to ground state (I_f, M_f) via intermediate state (I, M).

assumes that there is no external electric and magnetic field interacting with the nucleus. In the case of the presence of one of these fields, the angular correlation function is perturbed and thus needs to be expressed differently:

$$W(\theta, t) = \sum_{k=0}^{k_{max}} A_{kk} G_{kk}(t) P_k(\cos\theta) \tag{4.8}$$

where t is the time between emission of γ_1 and γ_2, and $G_{kk}(t)$ are the perturbation functions, which depend on the details of the nuclear interaction with the field.[35]

For most practical cases, the maximum value of k is 4, having $A_{4k} << A_{2k}$. For this work, in which the spin used is $I = 5/2$, the interaction studied is between the nuclear quadrupole moment and the EFG, so the perturbation function has the form:

$$G_{2k}(t) = S_{20}(\eta) + S_{21}(\eta)\cos(\omega_1 t) + S_{22}(\eta)\cos(\omega_2 t) + S_{23}(\eta)\cos(\omega_3 t) \tag{4.9}$$

The ratio ω_2/ω_1 is a function of the asymmetry parameter. The frequencies satisfy the equality $\omega_3 = \omega_1 + \omega_2$. The amplitudes S_{2i} depend weakly on the asymmetry parameter.[35],[36]

4.3 TDPAC spectroscopy

A TDPAC spectrometer is a device used to measure the angular correlation as a function of time between the emissions of γ_1 and γ_2.

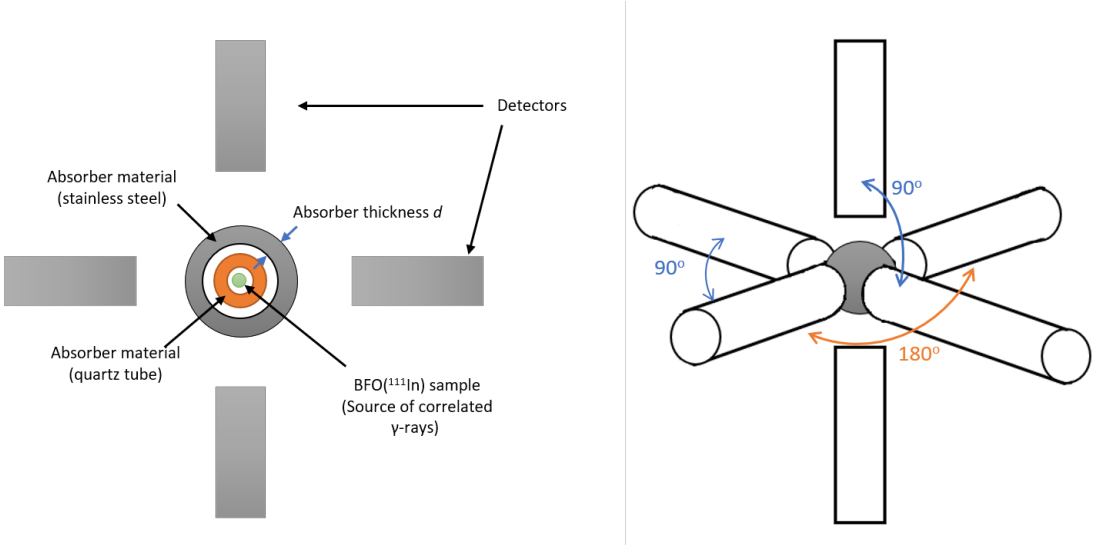

Figure 4.3: Schematic figures of simple TDPAC spectrometer setups. (Left) 4-detectors setup (based on literature[35]) and (right) 6-detector setup.

The spectra ratio R(t) is a combination of the four coincidence spectra. By design, the exponential decay term and the detector efficiencies cancel out. The probability of coincident detection of γ_1 in one detector and γ_2 in another detector is given by:

$$P_{\text{coin}}(t) = \frac{1}{\tau_{1/2}} \exp\left(-\frac{t}{\tau_{1/2}}\right) e_1 e_2 W(\theta, t) \tag{4.10}$$

where $\tau_{1/2}$ is the intermediate state life time, e_1 and e_2 are the detector efficiencies, which are very close so it can be assumed as being the same value.

Combining 12 coincidence spectra for four detectors, or 30 coincidence spectra for 6 detectors, the ratio is obtained[37]:

$$R(t) = 2\frac{W(180°, t) - W(90°, t)}{W(180°, t) + 2W(90°, t)} = A_{22} G_{22}(t) \tag{4.11}$$

where A_{22} refers to the experimental anisotropy coefficient of the $\gamma_1 - \gamma_2$ cascade and $G_{22}(t)$ is the theoretical perturbation factor $G_{22}(t)$ folded with the time-resolution curve of the spectrometer[38].

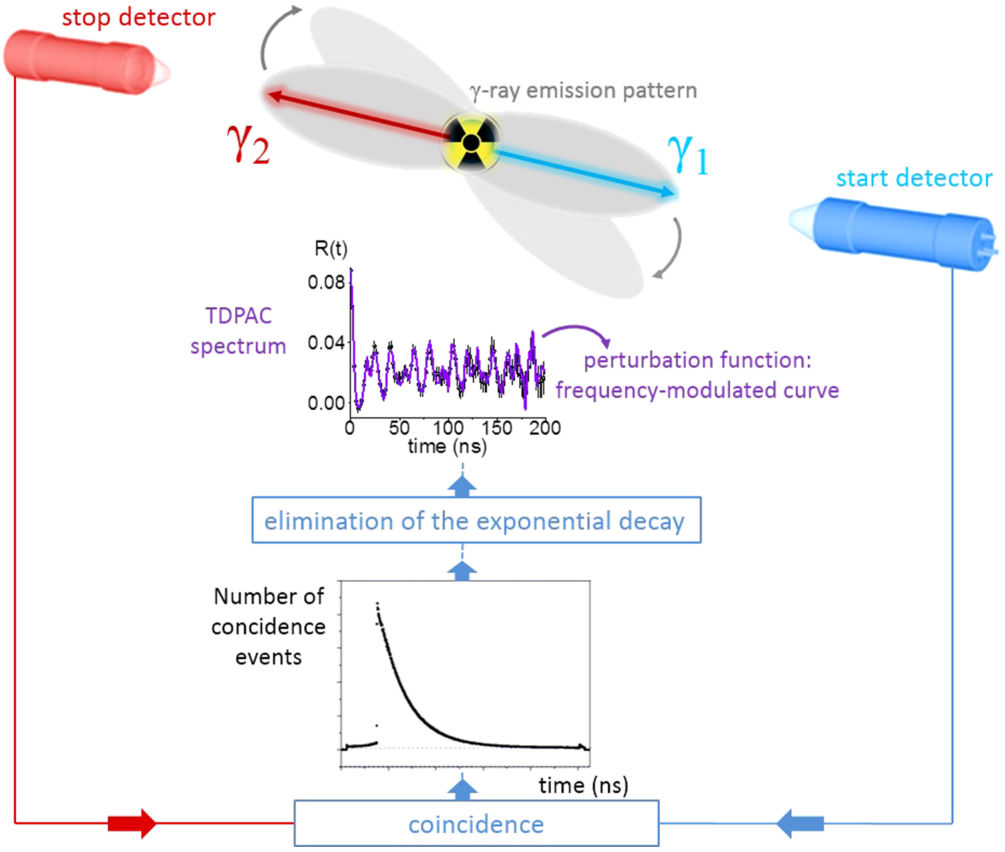

Figure 4.4: Schematic figure showing the TDPAC technique and data collection. Taken from literature.[39]

4.4 Effective anisotropy coefficient (A_{eff})

It is defined as effective anisotropy coefficients ($A_{\mathtt{eff}}$) the product of a correction Q_{kk} factor multiplied by the theoretical values of the A_{kk} factors[40]. The theoretical A_{kk} values depend on the decay cascade characteristics, such as the spins and multipolarity mixing of the emitted γ rays. The correction Q_{kk} is defined as the product of $Q_k(\gamma_1) \times Q_k(\gamma_2)$[41], and in the same way, the theoretical A_{kk} factors are the product of $A_k(\gamma_1) \times A_k(\gamma_2)$[42]. The Q_k attenuation factors have values between 0 and 1 and can be analytically estimated by integrating a normalized Legendre polinomial of order k within the acceptance geometrical solid angle of the scintillator of the TDPAC spectrometer, considering the efficiency for the photo peak creation that depends on the γ energy and the type of scintillator.

Unfortunately, the $A_{\mathtt{eff}}$ calculation does not always give us an $A_{\mathtt{eff}}$ value close to the experimental one. Source size effects, the centering of the sample and other aspects taking into account the light yield of the scintillator and photomultiplier characteristics make a simple analytic estimation of Q_k biased, easy increased by more than 30% of what it should be.

Therefore, an accurate way to estimate the right value is to measure the $A_{\texttt{eff}}$ value with a reference solution. Figure 4.5 shows the R(t) functions and their maximal amplitude (effective A_{22} values). Three different measurements were carried out in the same experimental conditions, which were performed for checking the reproducibility of the experiment.

Figure 4.5 shows that $A_{22\texttt{eff}}$ is the maximal amplitude of the observed TDPAC signal for a given probe, a given sample-detector geometry, and a given spectrometer. The effective A_{22} can be estimated by calculations, but it can also be measured. For the measurement a very small drop of $^{111}InCl_3$ in dilute hydrochloric acid was used, placed in a small test tube between the BaF_2 detectors of the K1 TDPAC spectrometer. Here the distance between the sample and the detectors was 3.5 cm. Due to the phenomenon of motional narrowing, the $^{111}InCl_3$ in the solution moves very fast, creating an almost undisturbed spectrum and thus, $A_{22\texttt{eff}}$ can be determined effectively.

One should also take into account that not only the solid angle Q_{kk} influences the $A_{22\texttt{eff}}$. Scattering in the sample (such as *intrasource scattering*) can also affect the $A_{22\texttt{eff}}$. However, this is only important for *"thick"* samples or for samples with a high Z. If more than one fraction is observed in the spectrum, the individual amplitudes must add up to $A_{22\texttt{eff}}$. In this case, missing fractions that for example can be related to remaining implantation damage, may be identified if $A_{22\texttt{eff}}$ was accurately estimated.

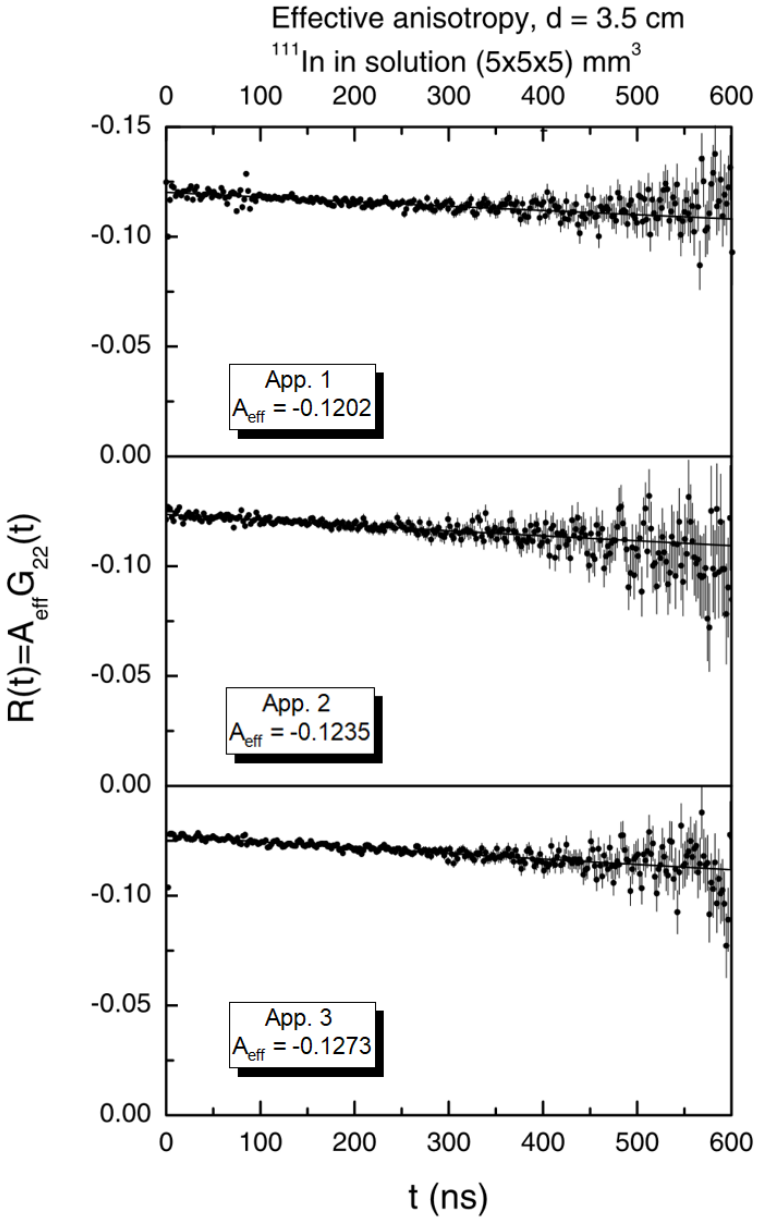

Figure 4.5: R(t) spectra taken for determination of effective anisotropy value ($A_{\mathtt{eff}}$) at the K1 machine[43].

Chapter 5

X-ray diffraction (XRD)

The technique of X-ray diffraction (XRD) is used for the study of the crystalline structure of materials in the macroscopic scale, as opposite to the TDPAC technique. It also provides information about the composition and about the unit cell dimensions, i.e. the lattice parameters.[44] This is possible because the X-ray wavelengths, which are between 0.2 and 10 nm, are comparable to the interatomic spacing of crystalline solids. The technique measures the average spacing between layers or rows of atoms.[45]

The atomic structure of crystalline materials, upon irradiation with X-rays, causes a constructive and destructive interference of the scattered X-ray beam. This generates a unique diffraction pattern which presents many sharp spots, known as Bragg diffraction peaks.[45]

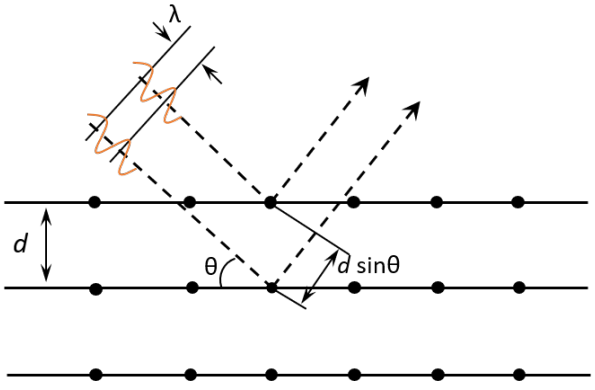

Figure 5.1: Schematic figure of Bragg diffraction.

When the scattered waves interfere constructively, they stay in phase since the difference between the path lengths of the two waves is equal to an integer multiple of the wavelength. This phenomenon is described by Bragg's law[46]:

$$2d_{hkl} \sin\theta = n\lambda \tag{5.1}$$

where d_{hkl} is the interplanar distance at the lattice plane hkl, θ is the angle of incidence, n is a positive integer and λ is the wavelength of the incident wave. Figure 5.1 shows these parameters with a schematic figure.

The Miller indexes (hkl) specify the orientation and spacing of the "reflecting" lattice plane, and it helps to determine the lattice parameters. For example, for a cubic unit cell the relation between the atomic layer spacing d_{hkl} and the lattice parameter a is given through

$$d_{hkl} = \frac{a}{\sqrt{h^2 + k^2 + l^2}} \tag{5.2}$$

X-Ray Diffraction measurements can be done in different ways, such as on single crystals, polycristalline materials, through powder diffraction or on bulk material. Moreover, there are different geometries of the source-sample-detector arrangement.

Chapter 6

Experimental details

The BFO samples were prepared at the University of Duisburg-Essen, and the ion implantation took place at the Bonn Radioisotope Separator and Implanter (BONIS) facility, in Bonn, Germany[47]. After the ^{111}In implantation, the sample was shipped to the Ion Separator OnLine DEvice (ISOLDE) facility[48], at the European Organization for Nuclear Research (CERN), where the full TDPAC study took place within the department of ISOLDE solid-state physics[49]. The pellet of BFO was cut into different pieces, allowing experiments in different TDPAC spectrometers for checking the reproductibility of the TDPAC measurements.

The polycrystalline BiFeO3 samples were synthesized at the University of Duisburg-Essen from a stoichiometric mixture of finely powdered bismuth oxide (Bi2O3, 99.9% Acros Organics) and iron oxide (Fe2O3, 99.99% Alfa Aesar). Following a calcination process for 3 hours at 820°C, the powder was pressed to pellets and sintered for six hours under air atmosphere again at 820°C.[2]

6.1 Ion implantation at BONIS, HISKP

The samples were implanted with the radioactive isotope ^{111}In at the BONIS facility, located at the Helmholtz-Institut für Strahlen-und Kernphysik (HISKP)[47],[50]. This facility stands out for the wide range of energies available for the ion acceleration, from 0.5 to 160 keV, allowing for the study of materials from the surface to depths of several nanometers. The facility counts with a cycloton, that provides radioisotopes for implantation. The ^{111}In isotope was implanted with an energy of 80 keV and using a commercially available liquid solution of $^{111}InCl_3$. Refer to the literature[50] for further details into the process of ionization of ^{111}In. Once this was achieved, the ionized elements are extracted to the ionization chamber and focused and accelerated at an energy of 80 keV. A Faraday cup and a probe oscillator are used to control the intensity of the ion fluxes implanted. Up to 5 samples can be mounted in the implantation holder simultaneously, so there is no need to break the system vacuum after each implantation.

It was briefly mentioned in chapter 3, that simulations of the implantation depth were performed using the SRIM software[28] using these parameters, and it gave an ion implantation depth of 221 Å. For a technique as precise as TDPAC, this depth already means that the surface of the sample is not accounted for in the measurements. Furthermore, a beam sweep was done during the ion implantation. This means that the probe was very homogeneously distributed along the sample, and not concentrated in one small portion. By doing the beam sweeping, it was possible to divide the sample in pieces that were used for measuring in different TDPAC spectrometers at the same time, and it can be well assumed that the concentration of ions implanted in all the pieces is the same. A picture of the sample pieces used for the TDPAC spectrometer KATAME can be seen in Figure 6.1.

Figure 6.1: Pieces of BFO sample.

For more information about the implantation process and the BONIS facility, refer to literature[47],[50],[51].

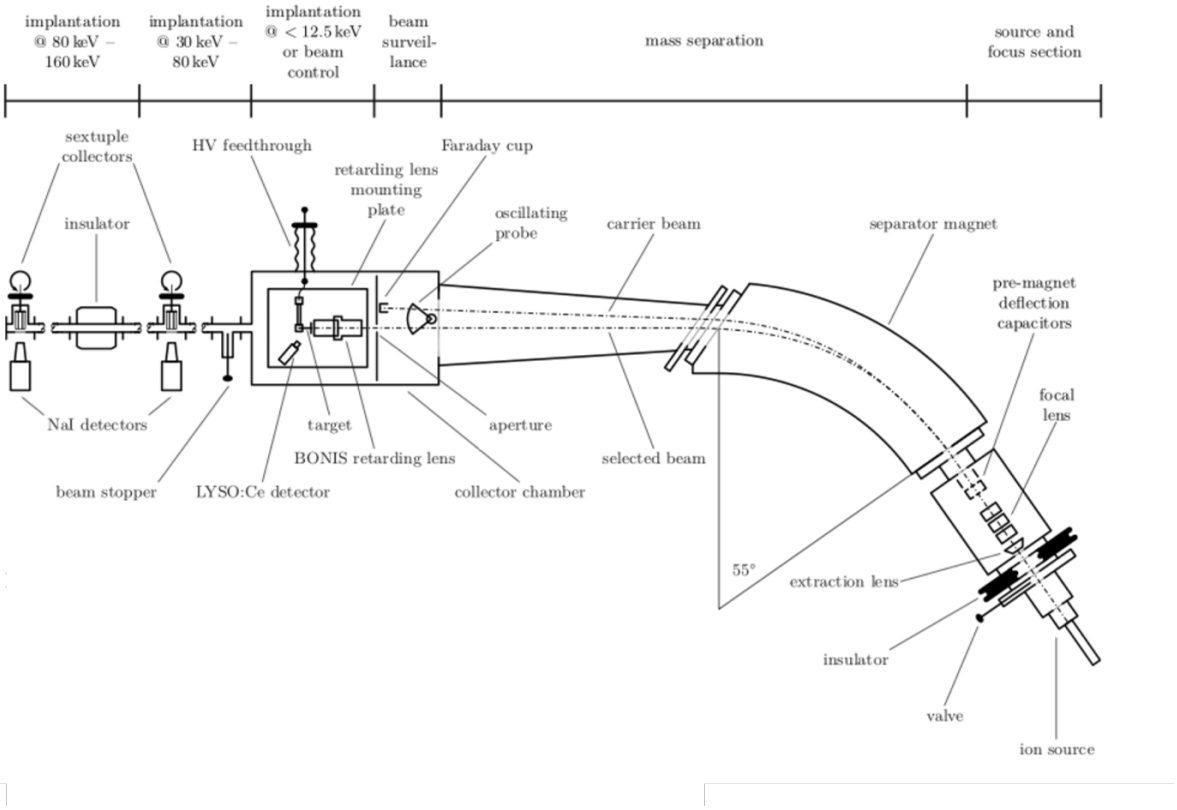

Figure 6.2: Sketch of the BONIS setup taken from literature[51].

6.2 TDPAC spectroscopy at ISOLDE, CERN

6.2.1 Experimental TDPAC spectroscopy setup

The measurement facilities at ISOLDE consist of several digital and analogue experimental TDPAC spectrometers with 4 or 6 gamma-detectors. A (4-/6-) detectors TDPAC spectrometer produces 12/30 coincidence spectra, not all similar. There are a set of similar spectra taken with detectors at 90 degrees and another set of spectra taken at 180 degrees. These two sets of spectra are combined to build the R(t) anisotropy ratio function[39].

There are two TDPAC spectrometers used for this work. The first one is a digital setup named KATAME (Fig. 6.3, left) and it consists of a 6-detectors with Lanthanum Bromide (LaBr3:Ce) scintillators mounted on XP2020URQ photomultipliers in cube arrangement. It is able to record the coincidence events of 30 independent detector combinations. The data collected from KATAME is directly digitalized and fed to the *PacSuit* software[52], which computes the energy spectra as well as the coincidence time histograms (more information in subsection 6.2.3). Additional information about digital 6-detectors TDPAC spectrometers can be found in the literature[53]. This TDPAC device was operated personally by me for the data treatment after the measurements had already taken place, whereas for the data of the second setup, the first step of data treatment (i. e. the time zero and background estimation) was previously performed and then sent to me to continue with the data analysis. The latter setup is an analogue spectrometer named K1 (Fig. 6.3, right), and it is based on a fast-slow delayed coincidence technique with four Barium Fluoride (BaF_2) detectors coupled on XP2020Q photomultiplier tubes, which are connected to a high voltage base.

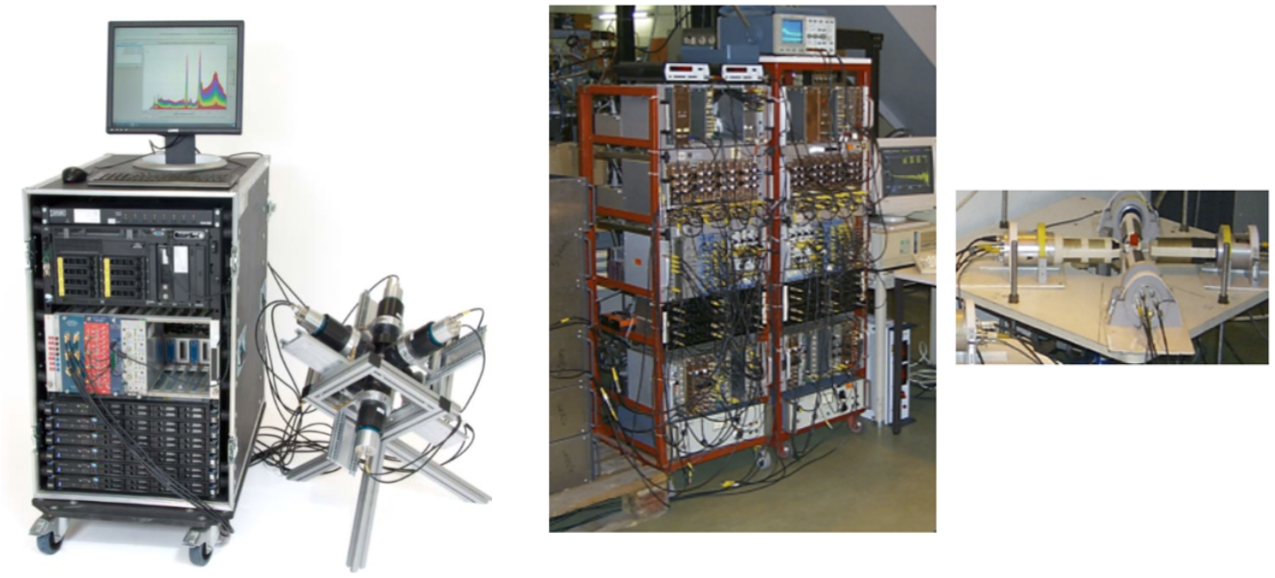

Figure 6.3: KATAME (digital 6-detectors setup) on the left[52] and K1 (analogue 4-detectors setup) on the right.[39]

With the water cooled furnace placed in the center of the detectors, high temperature measurements up to 840°C were performed. Furthermore, the pieces of the sample were placed inside a quartz tube with walls of 1mm thickness. The placement of this tube can be seen in Figure 4.3.

To be able to measure at high temperatures, the furnace was supplied with two Delta Elektronika SM7020 power supplies. The temperature was controlled manually through voltage adjustments so that the temperature signal, given by a NiCr-Ni thermoelement placed directly inside the furnace, could be stabilized. All measurements were performed under air atmosphere and without prior annealing.

6.2.2 TDPAC measurements

The same effective anisotropy coefficient were used for both TDPAC spectrometers:

$$\begin{aligned} \text{A22} &= -0.1222032 \\ \text{A24} &= -0.0904066 \\ \text{A42} &= -0.00051 \\ \text{A44} &= -0.0003773 \end{aligned}$$

These parameters were simulated for K1, considering ^{111}In as a probe and the detectors at 3 cm from the sample, with the assumption that the detectors are made of BaF_2 with $1.5''$ ($\sim$ 3.8 cm) diameter and $1.5''$ length.[54] An mAkk Fortran program written by J. G. M. Correia and J. G. Marques based on the literature[41],[42] was used for the computations.

The order and duration of each temperature measurement for both TDPAC spectrometers is shown in Tables 6.1 and 6.2. They were performed by the team of ISOLDE solid-state physics[49], CERN, during October-November 2019. For KATAME, the first measurements, after one at RT, were taken at high temperatures in ascending order until passed the Curie temperature point ($T_C \approx 822-829$°C). It is important to mention, that at high temperatures the TDPAC furnace counts with an uncertainty of ± 5°C. For K1, and after one measurement at RT, the two main temperatures setting the limits of the phase transition study were made: the lower limit, 800°C and upper one, thought to be enough to complete the phase transition, 840°C. At high temperatures, secondary phases such as $Bi_2Fe_4O_9$ are observed in BFO[2]. The first two measurements were performed at high temperature in order to investigate the effect caused on the spectra by the BFO decomposition. After these main measurements, the next ones were made in increasing steps from 649°C to 835°C.

Since the ^{111}In activity after the implantation was higher than expected, it was possible to carry out additional measurements. Thus, at the beginning only the temperature range to study the $\alpha - \beta$ phase transition was measured, and afterwards, more measurements took place decreasing the temperature from 600°C to 340°C (KATAME), 360°C (K1) to study the behaviour of the material below the Néel temperature ($T_N \approx 370$°C). After the last measurements, ^{111}In decayed to stable Cd. Therefore it was not possible to characterize the T_N transition, as there were not enough data points below the Néel temperature. Future

experiments below the T_N are foreseen as a part of the project "Local Probing of Ferroic and Multiferroic Compounds, IS647"[55].

KATAME					
Order	Temp. [C]	Duration [h]	Order	Temp. [C]	Duration [h]
1	RT	6	13	BREAK	4.66
2	650	4	14	600	7
3	700	4	15	550	15
4	750	4	16	500	16
5	800	6	17	450	12
6	807	6	18	400	17
7	810	4.66	19	380	14.66
8	814	7	20	370	20
9	818	7	21	360	17
10	822	7	22	350	49.5
11	829	8.5	23	340	117
12	835	8.66	23	RT	n/a

START	STOP
23-10-19	09-11-19

Table 6.1: KATAME order and duration of measurements.

K1					
Order	Temp. [C]	Duration [h]	Order	Temp. [C]	Duration [h]
1	RT	3	13	829	14.75
2	800	12	14	835	15
3	840	12	15	600	17.75
4	649	4.33	16	550	23.25
5	700	8.5	17	400	23.33
6	750	6	18	380	26
7	800	10	19	370	43
8	807	10	20	360	118
9	810	11	21	RT	56
10	814	10.5	*sample has decayed*		
11	818	9.5			
12	822	15			

START	STOP
23-10-19	11-11-19

Table 6.2: K1 order and duration of measurements.

6.2.3 Data Collection and treatment

Both spectrometers are based on the same principles, although KATAME is a digital machine, while K1 is an analog setup. The time signal is taken from the anode, while the energy signal for the slow branch is taken from the dinode. For K1, a logical signal is generated once a coincidence occurs between the energy and the timing signal, which is then used as an input for the logic units. A combination with the coincidence signals of the other detectors is handled. The start detector detects the first γ-ray (γ_1) and the stop detector detects the second γ-ray (γ_2). The hyperfine interactions exercise a torque on the angular momentum of the intermediate state of the probe. This produces a precession of the γ emission pattern, around the symmetry axis, as can be seen in Figure 4.4. With the combination of (4-/6-) detectors, positioned as shown in the schematic figures from Figure 4.3, it is possible to measure 12 (K1) and 30 (KATAME) coincidence spectra. The first data treatment step consists on eliminating the irrelevant variables, such as the exponential decay of coincidence spectra, time shifts and background estimation. Once this is done, the perturbation function is formed.

The data acquisition of K1 was done with the software UNCPACSB[56], whereas the background and time zero determination was performed with the software Interlude[57].

In the case of KATAME, this was done with the software *PacSuit*[52]. Within this software, the application *SpectraPac* provides a graphical user interface and it is used for the final data collection, as it provides as output the TDPAC spectra perturbation function (R(t)) at the different temperatures.

For the data analysis, different software were used, such as Nightmare (NNFit)[58],[59], GFit[60] and PacFit[52]. While NNFit is very effective to obtain the different hyperfine parameters for high temperatures, it is not so effective with the data analysis of temperatures below the Néel temperature. Thus, the data analysis of the temperatures range $T < T_N$ has to be made with the software PacFit. However, the fitting of combined hyperfine interactions is very complex and this analysis is foreseen as a future step.

Moreover, GFit was used to obtain the Fast Fourier transform (FFT) from the data obtained with NNFit.

6.2.4 Data collection and treatment with KATAME

To have a better idea of how the digital spectrometer setup works, the software used for the data collection is going to be better described. The *PacSuit* software[52] consists on three applications:

- *PacMan* (non-GUI): it can be controlled remotely. It only displays a console with output of statistics and diagnostic messages. It is used for the data collection from the digitizer, waveform processing and data dispatch via netwrok.
- *PacMaster*: it remotely configures the recording hosts and collects, sorts, compresses and saves the data. Diverse monitoring data is displayed: online energy spectra, sam-

ple waveforms, and statistics. It collects the coincidence spectra from *PacMan* and combines them.

- *SpectraPac*: (Offline): it has per-detector energy calibration, allowing for the selection of energy level windows and channel numbers, does an improved correlation search, determines background levels and each correlation spectrum's exact on-set time, and calculates the ratio spectrum and its Fourier transform. It only needs the data file saved by *PacMaster* to work - it can be used from any device. (Online): it can also do an online evaluation of data files while still running, making it easier to monitor in case the program needs to be stopped.

SpectraPac was the main application used for the generation of the frequency-modulated curve R(t), once the measurements were done. It was used to compute the energy calibration, energy discrimination, correlation analysis, R(t) calculations and Fourier transformation[52]. The data extracted was then imported into other software[58],[59],[60], to further extract the hyperfine parameter values and complete the study.

6.3 XRD

In the previous research using ^{111m}Cd,[2] an XRD study was made in the temperature range of the $\alpha - \beta$ phase transition to support the conclusions about the crystal symmetry made with the TDPAC technique. In principle, it would be not necessary to carry on this study in the same temperature range, since the samples were produced using the same method. However, the measurement duration of the TDPAC experiments performed with ^{111m}Cd is different from the ones performed with the ^{111}In probe. Therefore, XRD experiments were also performed. Moreover, as it can be seen in Table 6.2, the first measurements taken with the TDPAC spectrometer K1 were much longer in duration. This was done in order to study the thermal behaviour of BFO, meaning, the presence of secondary phases at high temperatures.

Thus, the first measurements were taken at very high temperatures, and they were left longer time in order to obtain a bigger percentage of secondary phase. It is expected that the XRD results reflect this outcome.

The XRD measurements were performed in the samples at the University of Duisburg-Essen, in Germany, before the ion implantation and after the TDPAC spectrometry.

Figure 6.4: BFO pellet before ^{111}In implantation.

Chapter 7

Results and discussion

There are two data sets involved in this research, and both were collected at the ISOLDE solid-state physics facilities[49], CERN. The first data set was collected by using KATAME, and the second data set, by K1 (refer to Section 6.2 for more information about the TDPAC setups).

It was mentioned that the nuclear probe chosen for the implantation was the radioactive isotope Indium-111, which half life (2.83 days) allows for many different measurements using the same sample. Hence, numerous measurements were done in the range of temperatures mentioned in Tables 6.1 and 6.2.

It is also important to mention again previous research using BFO with ^{111m}Cd implantation, which shares the intermediate level with our probe and thus both research can be compared. The interest in this comparison will be more clear when the results are explained.

Moreover, XRD diffraction measurements results are introduced to study the effect of thermal treatment on the sample pieces.

7.1 TDPAC measurements

As explained in Section 6.2, both TDPAC setup measurements follow an order divided in two main sets: an increasing in temperature until reaching temperatures above the Curie Temperature ($\sim 650 - 835$°C (KATAME), 840°C (K1)), and then a decreasing in temperature until reaching temperatures below the Néel temperature ($\sim 600 - 340$°C (KATAME), 360°C (K1)).

In this section, the results from the fitting of the R(t) spectra and the Fast Fourier transform (FFT) are presented for both temperature ranges and TDPAC spectrometers. The FFT analysis is a helpful tool to visualize the R(t) function through the transition frequencies ω_n and their ratio.

7.1.1 Spectra from 650°C to 835°C

During this temperature range, the phase transition from the α-phase to the β-phase is reached. In the R(t) spectra seen in Figure 7.1 and 7.2, it can be seen that once T_C is reached at ~ 829°C, the frequency-modulated curve, R(t), changes completely. Again, it is important to keep in mind that at high temperatures the TDPAC furnace counts with an uncertainty of ± 5°C. This uncertainty explains the offset in the $\alpha - \beta$ phase transition temperature for K1 and KATAME machines. Another explanation would be that the duration of the thermal treatments has affected (delayed) the transition to the β phase.

The first R(t) patterns, which appear until 829°C for KATAME spectra and until 822°C for K1 correspond to the α phase. An abrupt change in R(t) to the β phase is observed at 835°C for KATAME and 829°C for K1.

Looking at the fast Fourier transform (FFT), only one EFG at each phase can be observed, which is a sign of a first order transition. Furthermore, there is a clear difference between the EFGs of the α and β phase, visible through the quadrupole interaction frequency and their symmetry (EFG_α is symmetric, whereas EFG_β is not). As it is visible on the FFT of EFG_α, the low value of η close to zero leads to a $\omega_1 : \omega_2 : \omega_3$ ratio of $1 : 2 : 3$, which is expected as explained in section 4.1.

In the R(t) spectra in these figures also show that the transition frequency does not change regardless of the TDPAC spectrometer used for the measurements, digital (KATAME) or analogue (K1), and the frequency value keeps constant throughout the α-phase with a frequency of approximately 60-70 Mrad/s.

Moreover, the spectra obtained does not show signs of the appearance of the secondary phase $Bi_2Fe_4O_9$, which should start appearing at high temperature due to the volatility of BFO[8]. This does not mean that the secondary phase is not present, but that the TDPAC technique cannot detect it under the present measurement conditions. This technique studies the local environment of the implanted probe, which as it was explained in chapter 3, was implanted at a depth of around 214 Å. When bismuth starts decomposing into secondary phases in BFO, it goes closer to the surface of the sample. For a technique as precise as TDPAC, a depth of 214Å is not considered the surface anymore, and thus the measurements do not account for the secondary phases. However, and as it will be mentioned later on, this phase does appear in the XRD measurements of the sample at high temperatures.

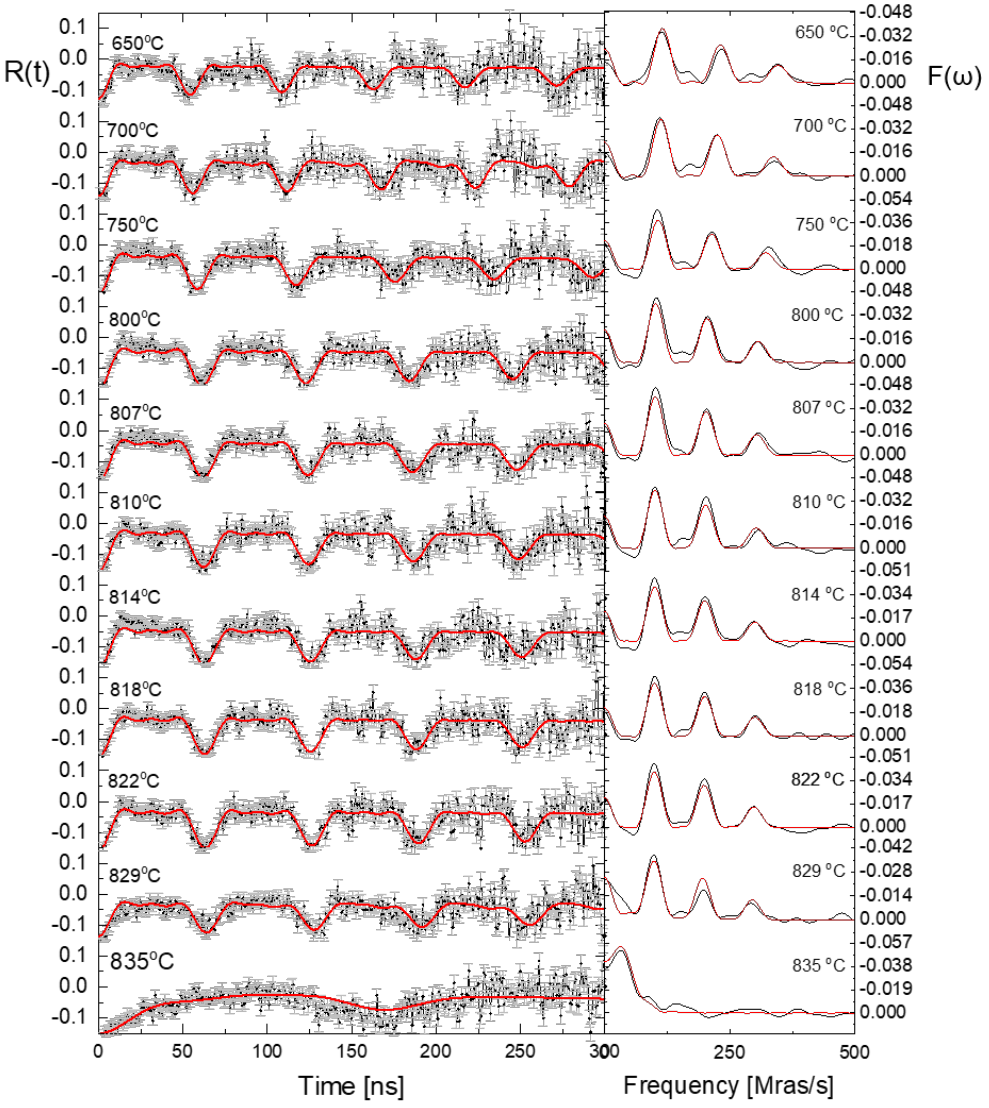

Figure 7.1: Left: KATAME spectra (symbols) and their fits (lines) and for temperature range $650 - 835°C$. Right: their corresponding Fourier Transform.

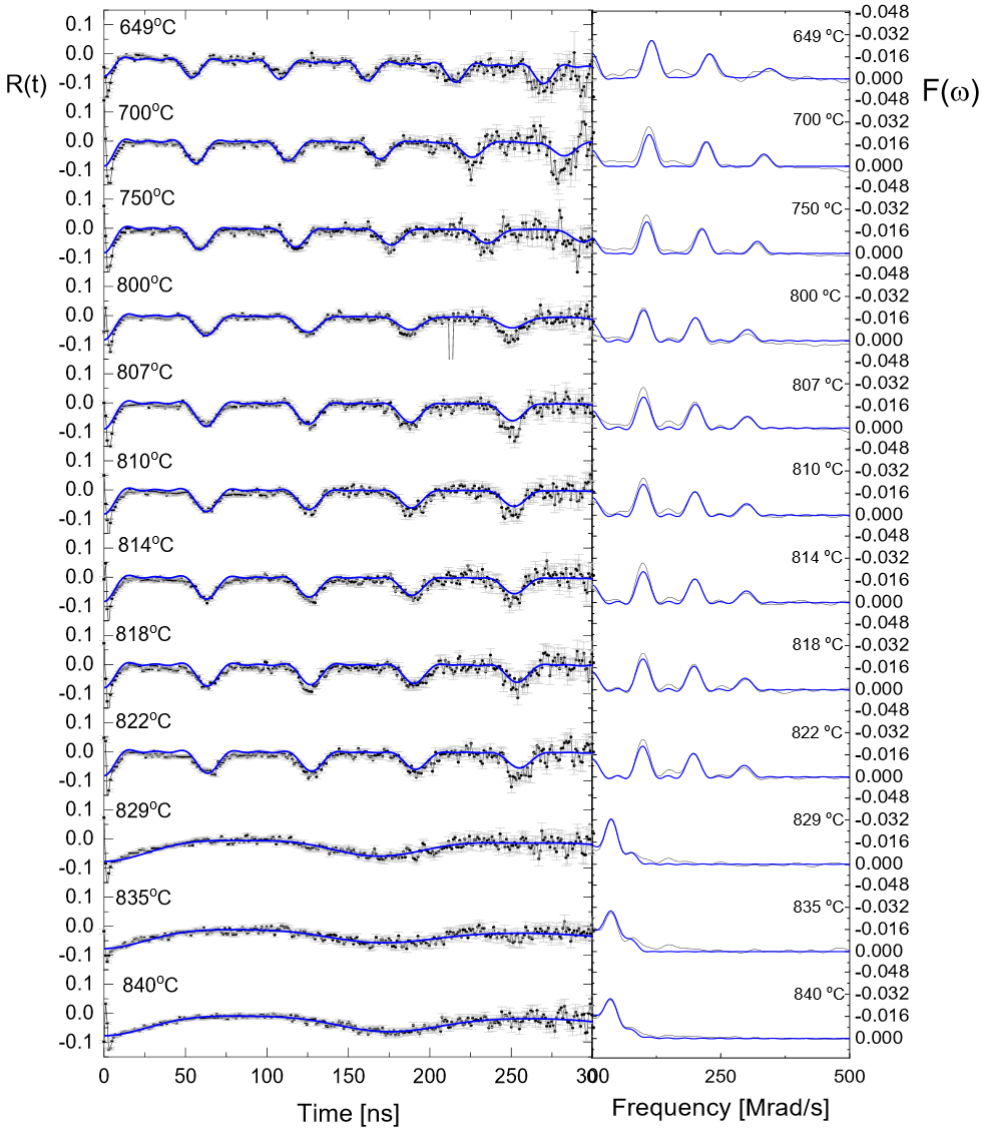

Figure 7.2: Left: K1 spectra (symbols) and their fits (lines) for temperature range 649 – 840°C. Right: their corresponding Fourier Transform.

7.1.2 Spectra from 600°C to 340°C

During this temperature range, the phase transition across the Néel temperature is reached at $T = 370°$. Below the Néel temperature, combined hyperfine parameters appear and the magnetic interaction is a factor to consider. Hence, the fitting of these temperatures is harder to do, and it needs different software and research. Unfortunately, the detailed fitting of this temperature range was not possible to performed during this work, although the unfitted spectra is shown in Figure 7.3.

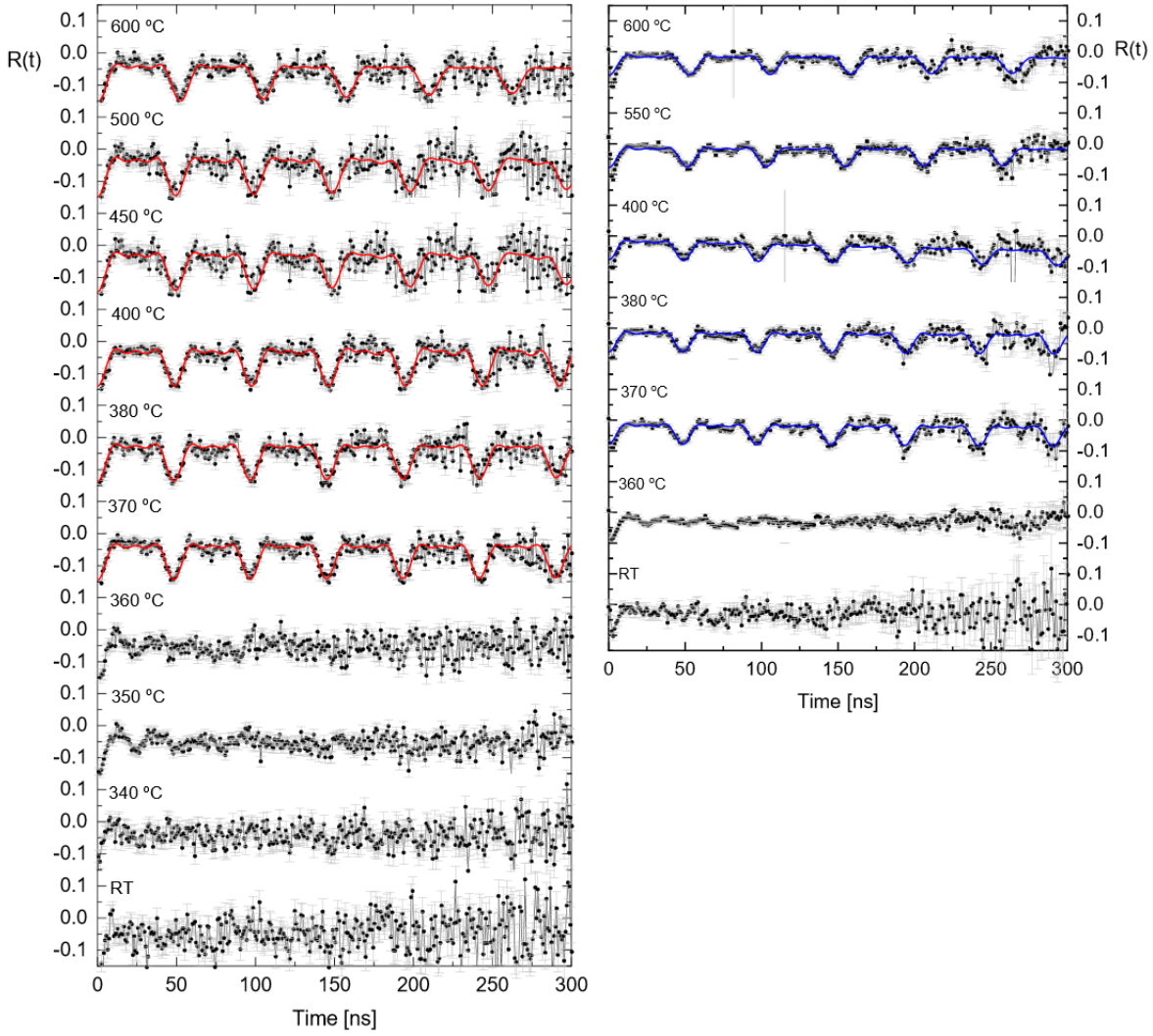

Figure 7.3: KATAME (red) and K1 (blue) spectra (symbols) and their fits (lines) for temperature range 600° C - RT.

7.1.3 Hyperfine parameters above T_N

In this section, different graphs showing the behaviour of the main hyperfine parameters (quadrupole interaction frequency ω_0, asymmetry parameter η and damping δ) are presented for the range of temperature above T_N. In Appendix A, tables A.1 and A.2 show all the hyperfine parameter values that are plotted in these graphs.

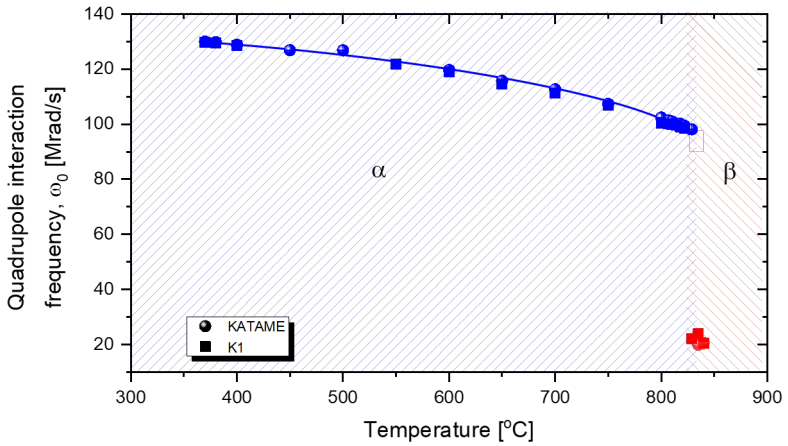

Figure 7.4: Temperature dependence of the observable frequency (ω_0) for KATAME and K1. The α-phase is shown in blue, whereas the β-phase in red. The error bars that can not be seen lay within the data symbols. The line is shown for visual guidance.

Looking at Figure 7.4, it can be seen that once the temperature of 829°C is reached, ω_0 *decreases*, indicating the transition to the β-phase. This also indicates that the Curie temperature for our experiments must be around this point. The sudden drop in the frequency is also proof of the first order transition from the α to the β phase in BFO. The reason for the difference in the value of the Curie temperature obtained here and the literature is due to the fact that the temperature point of phase transition in BFO depends on the particle size. This effect was observed for the T_N and was studied using Mössbauer spectroscopy[61]. Furthermore, it is important to know that the furnace used for the measurements, at high temperatures, have an uncertainty of ±5°C. This figure also shows that the values for ω_0 follow a parabolic trend during the α-phase, in which it decreases from an approximate value of 130 Mrad/s to 98 Mrad/s. This trend is fitted using Landau theory, which defines the EFG dependence on spontaneous polarization of the crystal up to T_C, following this expression[62]:

$$V_{zz} = \xi \cdot P_s^2 = \xi \cdot \frac{\beta}{2\gamma} \left[1 + \sqrt{\frac{1}{4} - \frac{\chi_0^{-1}\gamma}{\beta^2} (T - T_C)} \right] \tag{7.1}$$

with the definitions of the Landau expansion coefficients, $\alpha = \chi_0^{-1}(T_0 - T), \beta, \gamma$, according to the standard version found in the literature[63]. The temperature dependence of α is expressed in terms of the absolute temperature (T) and the Curie-Weiss law temperature T_0 (not to be mistaken with the Curie temperature T_C, which for a first order transition is given by $T_C = T_0 + \frac{3\beta^2}{16\chi_0^{-1}\gamma}$). The local EFG at the probe site is a result of the change in polarization. The change in polarization with change in temperature is related to the change of V_{zz}, and to further understand this change, the experimental data for P_s was used (taken from literature[62]) for fitting Equation 7.1 which directly results from Landau theory[64].

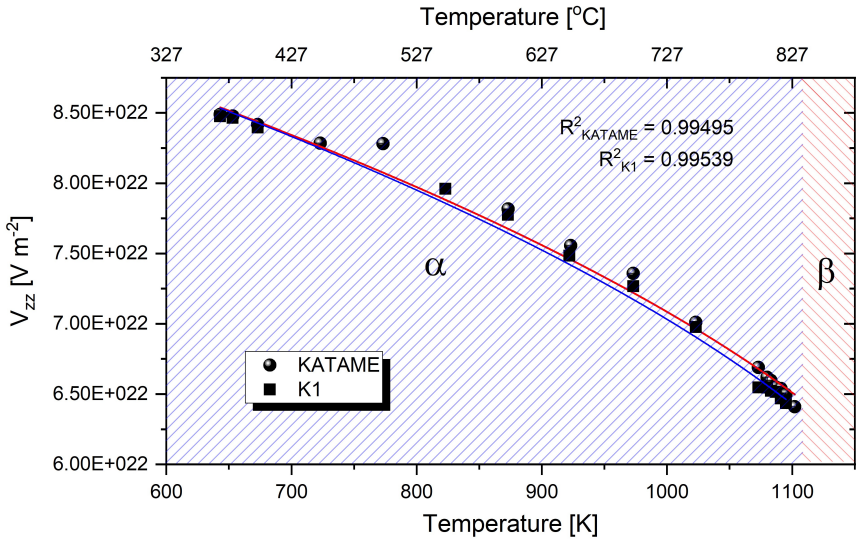

Figure 7.5: Temperature dependence of V_{zz} for KATAME and K1 and the line fitting using Landau theory. The α-phase is shown in blue, whereas the β-phase in red. The error bars that can not be seen lay within the data symbols.

The proportionality $V_{zz}^{Cd} = \xi \cdot P_s^2$ was fitted to the TDPAC parameters from the high temperature range during the α-phase yielding the values shown in Table 7.1. As it can be seen from this table, the R^2 values approximate to 1 for the fitting of both TDPAC spectrometers, meaning that the fitting curve is very accurate. This is an indication that the ^{111}In probe, even if not located at the Bi-site, is able to measure the polarization changes of BFO. Moreover, it could also mean that the Fe-site contributes to the local polarization. It is expected that the polarization comes mostly from the Bi-site[10],[9], but this does not discard the possibility of a small polarization contribution coming from the Fe-site.

Parameter	KATAME	K1
$\xi/2$ [V m^2 /(C)^2]	4.51E19 ± 1.05E17	4.46E19 ± 9.54E16
$\frac{\beta}{\gamma}$ [(C / m^2)^2]	959.58 ± 0	964.23 ± 0
$\frac{\chi_0^{-1}}{\beta}$[(C / m^2)^2/K]	1.45104 ± 0	1.52 ± 0
T_C [K]	1102	1095
T_C [°C]	829	822
R^2	0.99495	0.99539

Table 7.1: Parameters from Landau fitting obtained for KATAME and K1.

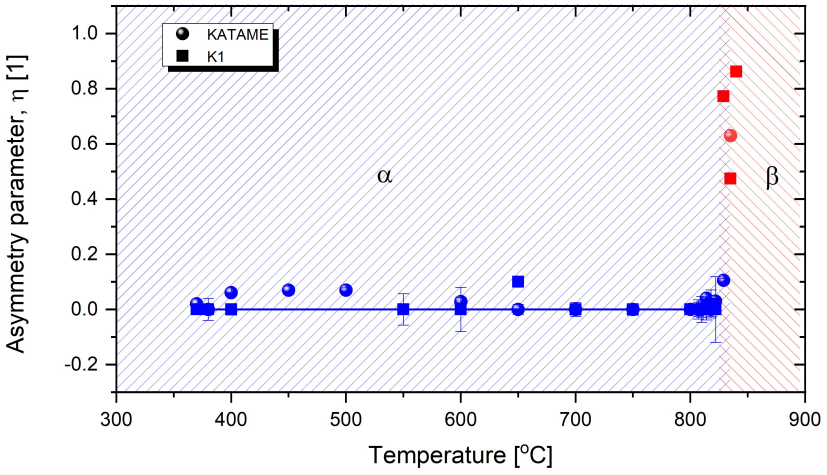

Figure 7.6: Temperature dependence of the asymmetry parameter (η) for KATAME and K1. The α-phase is shown in blue, whereas the β-phase in red. The error bars that can not be seen lay within the data symbols. The line across $\eta = 0$ is shown for visual guidance.

Looking now into Figure 7.6, where the asymmetry parameter values are shown, it can be seen that the crystal structure suffers a clear change in symmetry which, once again, matches with the EFGs values observed in the FFT. During the α-phase, the η values approximate 0 whereas for the β-phase these values are increasing and approximating to 1. Thus, the structure changes from being symmetric to an asymmetry state. It is an unusual phase transition on a perovskite structure (from rhombohedral $R3c$ to orthorhombic $Pbnm$), as an *increase* in symmetry from orthorhombic to rhombohedral with increasing temperature is more usual[8].

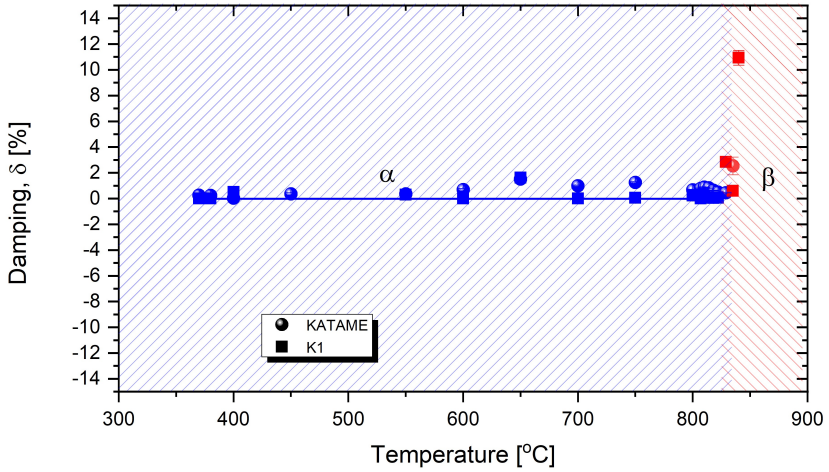

Figure 7.7: Temperature dependence of the damping parameter (δ) for KATAME and K1. The α-phase is shown in blue, whereas the β-phase in red. The line across $\delta = 0$ is shown for visual guidance.

The low asymmetry parameter observed for the α-phase, as well as the small damping, are due to small lattice imperfections[65], like counterrotations of adjacent oxygen octahedra about [111][1],[10], and is a reflection of the great sensitivity of the ^{111}In probe to deviations from axial symmetry while incorporated in a dilute regime in BFO.

The small values of the damping (δ) shown in Figure 7.7 indicates a rather narrow EFG distribution and it allows an accurate analysis. These small values are constant throughout the rhombohedral phase, whereas they start increasing when the structure changes towards the orthorhombic phase. Due to the fact that the damping values are close to 0 in most of the temperature points of the α-phase, the error estimated by the software[60] was very large and therefore the error bars have been removed from the graph.

7.2 XRD results

The set of XRD are separated into two measurements sets, the first one done right after the synthesis of the sample, and thus prior to the TDPAC measurements, and the second one after the TDPAC measurements, when the sample pieces have already been through the thermal treatment. In the last measurements, it is also necessary to make a distinction between the sample piece used with KATAME and with K1, as the thermal treatment was different during the TDPAC measurements. The data analysis was performed using the software HighScore Panalytical[66].

7.2.1 XRD measurements prior to TDPAC

Once the BFO sample was synthesized from a stoichiometric mixture of finely powdered bismuth oxide (Bi_2O_3) and iron oxide (Fe_2O_3), it was measured with XRD to study its purity. The result can be observed in Figure 7.8. Here, it can be seen that the calculated value expected for the pure BFO sample matches the experimental data result, which indicates that the sample does not have any secondary phase present. This is expected, as it was not yet put through to the thermal process.

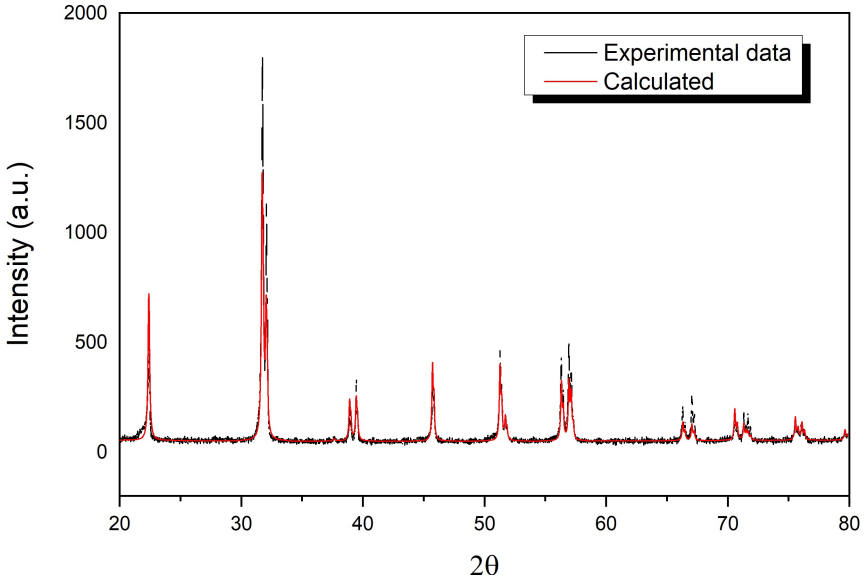

Figure 7.8: XRD measurement in BFO sample before TDPAC measurements.

7.2.2 XRD after TDPAC

The XRD measurements after TDPAC were done to see how the different thermal treatment affected the amount of secondary phase in the sample, specially $Bi_2Fe_4O_9$.

In Figures 7.9 and 7.10 it can be observed that the secondary phase $Bi_2Fe_4O_9$ is present in both pieces of sample, but in different quantities. The thermal treatment was longer in the piece used with the TDPAC spectrometer K1 (refer to Table 6.2 for more details about the duration of the measurements), and the results show that the percentage of secondary phase in this sample is larger than in the one measured with the TDPAC spectrometer KATAME. For the K1 sample the percentage of pure BFO is of 75.1%, and the percentage of $Bi_2Fe_4O_9$ is of 24.9%, whereas for the KATAME sample these values are 80.3% and 19.7%, respectively.

Thus, it is proven that the thermal treatment affects directly to amount of secondary phase present in the sample.

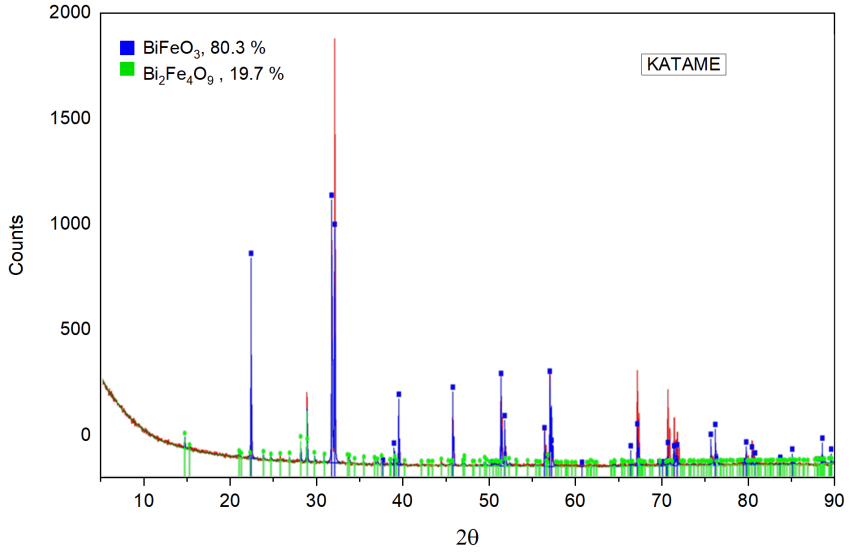

Figure 7.9: XRD measurements after TDPAC for KATAME.

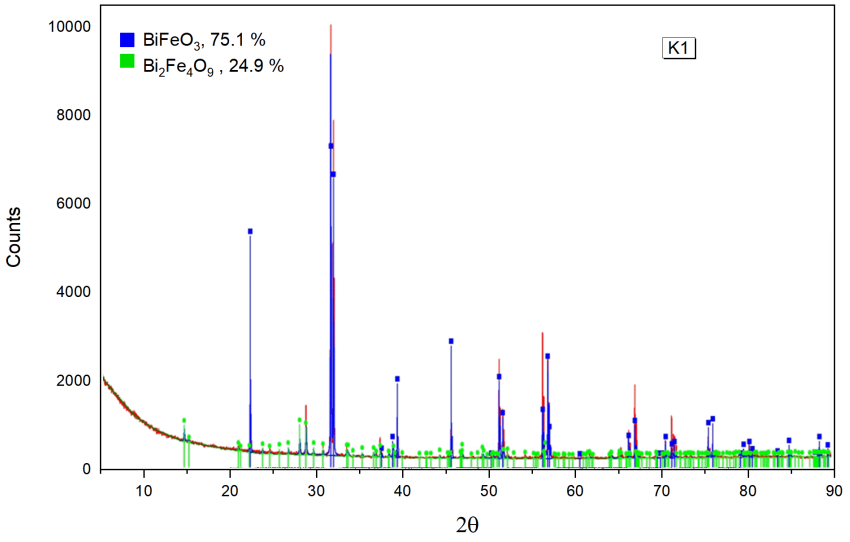

Figure 7.10: XRD measurements after TDPAC for K1.

Chapter 8

Data interpretation and discussion

To the best of our knowledge, there is no previous work reporting TDPAC measurements of BFO using ^{111}In as probe nuclei. Therefore, it is not possible to make direct comparisons. However, during this chapter different research relevant to the understanding of this report are presented.

8.1 ^{111}In vs ^{111m}Cd

The fundamental principles of this subsection are based on the reference ([2]): G Marschick et al. "Multiferroic bismuth ferrite: Perturbed angular correlation studies on its ferroic $\alpha - \beta$ phase transition". In:Physical Review B102.22 (2020), p. 224110

Previous research was done in the ISOLDE facility very similar to this one, but using ^{111m}Cd as nuclear probe (refer to Chapter 3 for more information). It was concluded that the probe was located in the A-site of BFO, substituting bismuth atoms. It was also concluded that there is a phase transition disorder interval in the temperature range of 804-829°, between the α and β phase. During this transition, it was detected the α-phase structure of *R3c* with a distortion seen as a "*forecast*" of the β-phase. Figure 8.1 (right) shows the spectra of BFO(^{111m}Cd), with the fitting line in green. The top graph with the spectra for $T = 800$°C shows the unaltered spectra of the α-phase. In the middle graph ($T = 822$°C), it can be seen that there is something happening in the spectra, as the Bi coordination is now disordered. This shows the phase transition described earlier, in which it is now more clear that the structure is going to change. In the bottom graph ($T = 831$°C), the β-phase has already been fully reached, so the structure is again unaltered, showing the space group *Pbmn*.

However, Figure 8.1 (left) shows the spectra of BFO(^{111}In) using KATAME. Here, the top graph is showing the unaltered spectra of the α-phase of BFO; and the bottom graph shows the unaltered spectra of the β-phase. However, the middle graph doe not show a $\alpha - \beta$ phase transition. Instead, it is still α-phase. As it was described in section 7.1.1, where the entire set of spectra of BFO(^{111}In) is analysed, there is a clear change between phases from the

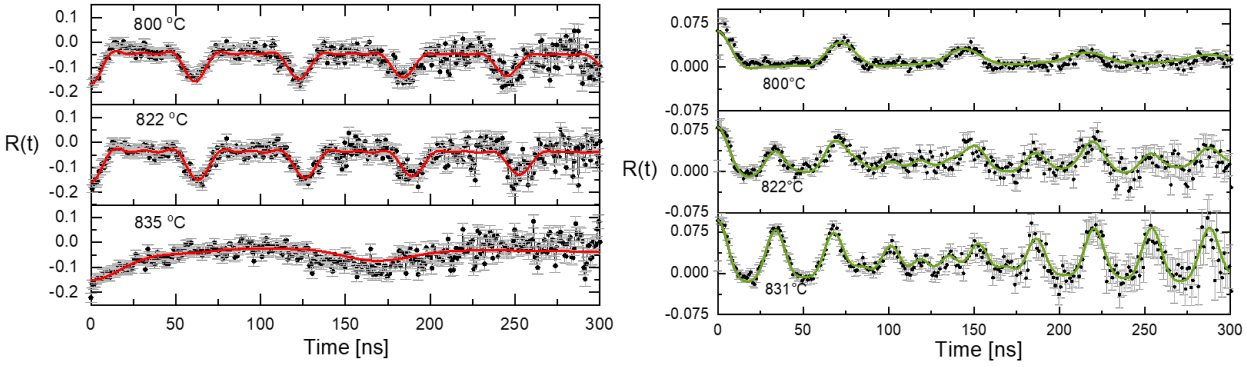

Figure 8.1: R(t) spectra comparing the phase transition of BFO(^{111}In) (left) and BFO(^{111m}Cd) (right).

measurement at 829°C to 835°C, in which the spectra shows the β-phase unaltered. It is important to mention the BFO(^{111m}Cd) spectra looks *upside-down* because the A_{22} value differ from the one of BFO(^{111}In) in a negative sign[26].

Comparing both spectra, it can be seen that using the probe ^{111}In the transition between the phases is of first order, whereas using ^{111m}Cd, a disorder interval exist between the α and β phase. Two explanations were given for the presence of this interval. The first was to assign it to the local coordination disorder of the Bi-atoms. The second explanation was the presence of polytype phases that acts as intermediate structures between the α and β phases.

Figure 8.2 shows the quadrupole interaction frequency for both research, BFO(^{111}In) and BFO(^{111m}Cd), as it is the most important hyperfine parameter to compare the results. Here it can be seen that for the α-phase the values of BFO(^{111}In) are higher than for BFO(^{111m}Cd), and that this changes drastically for the β-phase, where the frequency using ^{111m}Cd increases towards a value of $\sim$ 110 Mrad/s whereas for ^{111}In, it decreases to 20 Mrad/s. This might be due to the fact that the site occupation is different for both probes, thus ^{111m}Cd shows the behaviour of the A-site in BFO (substituting bismuth atoms), whereas ^{111}In occupies the B-site (substituting iron atoms). Moreover, during the research of BFO(^{111m}Cd) Density Function Theory (DFT) simulations were made using the Ab Initio Vienna Simulation Package (VASP). The results of these simulations can be found in the Appendix, Figure A.2. These results can also be used to analyse BFO(^{111}In) as both probes share the same intermediate state. Thus, the simulations show that the values of the hyperfine parameters of the Cd probe substituting the iron atoms (Cd @ Fe) are close to our results ($V_{zz} \approx 2.37/8.43[10^{21}/\mathrm{Vm}^2], \eta \approx 0.87/0.18[1], \omega_0 \approx 33.3 - 35.9[\mathrm{Mrad/s}]$), and hence it can be assumed that the ^{111}In probe is located in the B-site of BFO. The physics behind the different values of the hyperfine parameters depending on the location of the probes can be explained going back to section 2.2, in particularly to Figure 2.5, where it can be seen that for Bi-O the bond lengths become shorter and thus indicating that the atoms are closer at

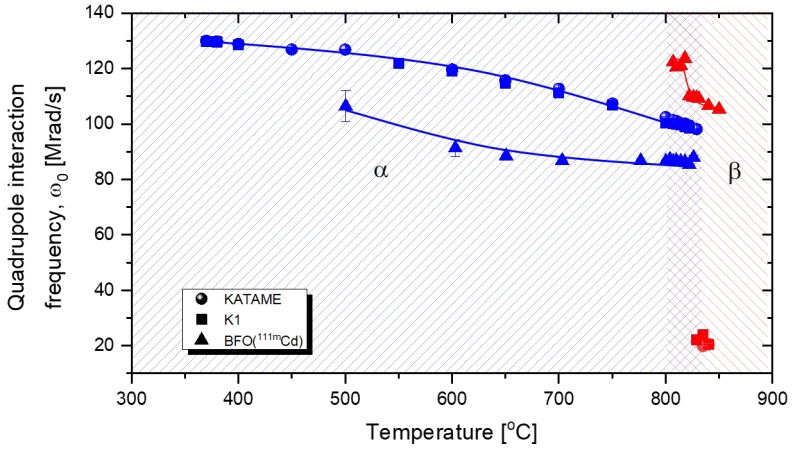

Figure 8.2: Quadrupole interaction frequency (ω_0) for BFO(^{111}In) and BFO(^{111m}Cd). The α-phase is blue, and the β-phase red. The error bars that can not be seen lay within the data symbols. The lines are shown for visual guidance.

all times, whereas for Fe-O three of the bond lengths become shorter, and three longer. As the behaviour of the ion bonds is so different, the results are expected to be clearly different as well.

Moreover, Figure 8.2 also shows that for ^{111m}Cd there is a temperature range in where a phase transition occurs (overlap between blue and red background), which is much bigger than the one for ^{111}In. Marschick et al.[2] explains this as an indication that the β-phase will happen soon, so the phase transition works as a *forecast* for the phase change. This is explained with the change in coordination of bismuth with respect to oxygen, which changes from a six-coordination in the α-phase to an eight-coordination in the β-phase. However, the octahedra of iron and oxygen does not change in coordination with temperature, so the phase transition interval cannot be clearly seen in our results considering that ^{111}In is in the B-site.

8.2 BFO doped with In

The fundamental principles of this subsection are based on the reference ([29]): GS Arya, RK Kotnala, and NS Negi. "Structural and multiferroic properties of $Bi_{1-x}In_xFeO-3$ ($0 \leq x \leq 0.20$) nanoparticles". In:Journal of Applied Physics113.4 (2013), p. 044107

Previous research consisting of the study of In doped BFO nanoparticles[29] is now briefly discussed. This research aims to improve the multiferroic properties of BFO by means of the cation size effect, as it is known that the substitution of bismuth atoms in BFO for rare earth ions improves these properties. It makes sense to think of indium ions to substitute bismuth, due to the smaller ionic radius of ^{111}In (refer to Table 3.2) and the fact that both In^{3+} and Bi^{3+} are non magnetic ions. During this research, the conclusion that the indium ions occupy the bismuth site is reached, although only XRD measurements are made, and the analysis

was only performed during the α-phase. Thus, it is not granted that the ^{111}In probe used in our project occupies the A-site in the BFO structure, as the main arguments used to define the site assignment have been taken from the information during the phase transition into the β-phase, and the β-phase itself.

8.3 Site assignment

*Reprinted figure with permission from Julian Gebhardt and Andrew M. Rappe "Doping of $BiFeO_3$: A comprehensive study on substitutional doping". 10.1103/PhysRevB.98.125202. Copyright (2021) by the American Physical Society. The fundamental principles of this subsection are also based on this study.

Substitutional dopants cause structural changes in the BFO structure. There is the direct effect of substituting ions of different sizes, as well as other secondary effects owing to the oxidation (p-type doping) or reduction (n-type doping) of iron centers, which causes changes in the oxygen octahedra. Therefore, the relaxation of the lattice cannot be only explained by the ionic radii difference. It is mainly related to the oxidation of the iron and the consequence of the decreased spatial requirements of the FeO_6 octahedra.

Highly oxidized cations in oxidation states of +3 and above prefer the B-site for most of the periodic table until the sixth period, i.e., up to cations that are almost as large as Bi^{+3} itself. As indium is part of the fifth period in the periodic table, it is part of the cations that prefer the substitution in the B-site of BFO. Furthermore, indium is part of group XIII, which are elements that form 3+ ions, donating valence s and p electrons to the oxygen valence band. From group XIII, only Tl^{+3} is large enough to prefer A-site substitution.

Figure 8.3 shows a graph listing the site preference for substitutional doping in BFO. The negative and positive areas correspond to the A-site and B-site, respectively. It can be seen that In^{3+} tends to substitute the B-site, corresponding to iron atoms. However, In^{+3} is shown right at the limit dividing the preference site occupation, thus it can actually substitute any of the sites. The concrete site assignment will then depend on other factors, as it could be the different between the EFGs of BFO(^{111m}Cd) and BFO(^{111}In) shown earlier.

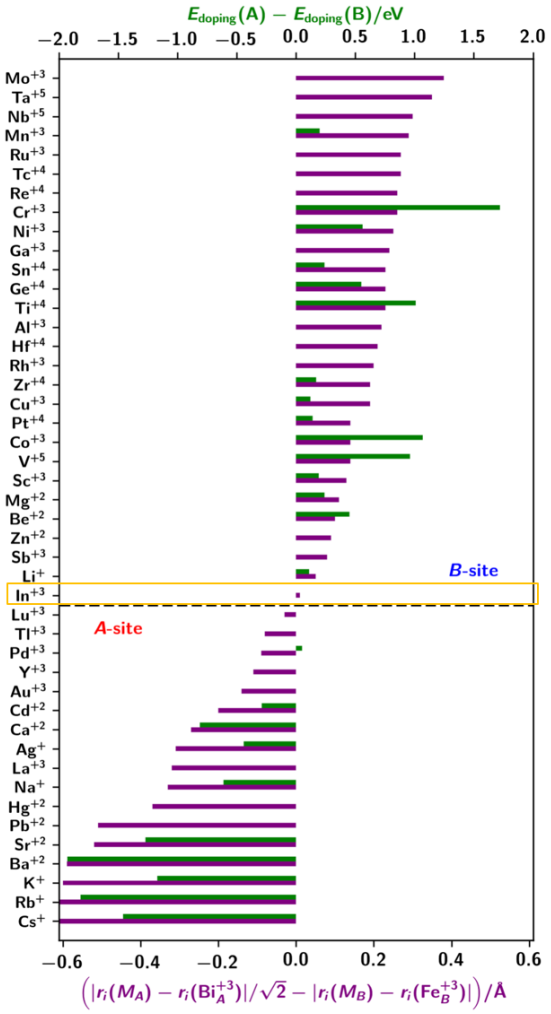

Figure 8.3: Site preference of different ions for substitutional doping in BFO according to ionic radii (purple) and DFT energies (green).*

Chapter 9

Conclusion

This work reports on TDPAC measurements in bismuth ferrite for the local environment investigation of the implanted nuclear probe ^{111}In. The measurements were performed as a function of temperature. The XRD measurements were performed before and after the TDPAC experiments, in order to verify the thermal treatment effect in the sample with respect to the amount of secondary phase that appears at high temperatures. Two TDPAC spectrometers were used for verifying the results reproducibility, one 6-detector digital setup named KATAME and one 4-detector analogue setup named K1. After the TDPAC measurements, it could be seen that both spectrometers gave very approximate results. These measurements, when compared to ab initio simulations from previous research[2], indicate that the nuclear probe is located in the B-site of the BFO structure, which corresponds to the substitution of iron atoms. This is shown by looking at the R(t) spectra which shows a first order transition corresponding to the change in crystal structure from *R3c* in the α-phase to *Pbnm* in the β-phase. An additional evidence is given by the fact that the octahedra formed by the iron and oxygen atoms in BFO do not change in coordination during the change in crystal structure from the α to the β phase, and thus there is no coordination disorder interval to be observed.

The XRD measurement have shown that the longer thermal treatment that took place during the TDPAC measurements using K1 created a bigger percentage of secondary phase ($Bi_2Fe_4O_9$) present in the sample, obtaining a 24.9% with K1 versus 19.7% present with KATAME, as the samples for this TDPAC spectrometer went through a shorter thermal treatment.

Future steps could include the TDPAC study of the behaviour of BFO(^{111}In) below the Néel temperature, which is an already foreseen step as part of the project "Local Probing of Ferroic and Multiferroic Compounds, IS647"[55].

Bibliography

[1] G Catalan and JF Scott. "Physics and applications of bismuth ferrite". In: *Advanced materials* 21.24 (2009), p. 2463.

[2] G Marschick et al. "Multiferroic bismuth ferrite: Perturbed angular correlation studies on its ferroic α - β phase transition". In: *Physical Review B* 102.22 (2020), p. 224110.

[3] Wikipedia. *Multiferroic materials*. Visited 2020. URL: `https://en.wikipedia.org/wiki/Multiferroics`.

[4] Nicola A Hill. "Why are there so few magnetic ferroelectrics?" In: *The journal of physical chemistry B* 104.29 (2000), p. 6694.

[5] Wikipedia. *Magnetoelectric Effect*. Visited 2020. URL: `https://en.wikipedia.org/wiki/Magnetoelectric_effect`.

[6] G Marschick. "Perturbed angular correlation and x-ray diffraction studies on the alpha-beta phase transition in multiferroic bismuth ferrite". MA thesis. Vienna University of Technology, 2020.

[7] Wikipedia. *Perovskite (structure)*. Visited 2020. URL: `https://en.wikipedia.org/wiki/Perovskite_(structure)`.

[8] DC Arnold et al. "Ferroelectric-paraelectric transition in $BiFeO_3$: crystal structure of the orthorhombic β phase". In: *Physical Review Letters* 102.2 (2009), p. 027602.

[9] SR Burns et al. "The Experimentalist's Guide to the Cycloid, or Noncollinear Antiferromagnetism in Epitaxial $BiFeO_3$". In: *Advanced Materials* 32.45 (2020), p. 2003711.

[10] JB Neaton et al. "First-principles study of spontaneous polarization in multiferroic Bi Fe O 3". In: *Physical Review B* 71.1 (2005), p. 014113.

[11] R Haumont et al. "Phonon anomalies and the ferroelectric phase transition in multiferroic $BiFeO_3$". In: *Physical Review B* 73.13 (2006), p. 132101.

[12] IA Kornev et al. "Finite-temperature properties of multiferroic $BiFeO_3$". In: *Physical Review Letters* 99.22 (2007), p. 227602.

[13] R Palai et al. "β phase and γ- β metal-insulator transition in multiferroic Bi Fe O 3". In: *Physical Review B* 77.1 (2008), p. 014110.

[14] R Haumont et al. "Phase stability and structural temperature dependence in powdered multiferroic $BiFeO_3$". In: *Physical review B* 78.13 (2008), p. 134108.

[15] SM Selbach et al. "The ferroic phase transitions of $BiFeO_3$". In: *Advanced materials* 20.19 (2008), p. 3692.

[16] J Wei et al. "Temperature-driven multiferroic phase transitions and structural instability evolution in lanthanum-substituted bismuth ferrite". In: *The Journal of Physical Chemistry C* 123.7 (2019), p. 4457.

[17] K Momma and Fujio Izumi. "VESTA 3 for three-dimensional visualization of crystal, volumetric and morphology data". In: *Journal of applied crystallography* 44.6 (2011), p. 1272.

[18] M Quirós et al. "Using SMILES strings for the description of chemical connectivity in the Crystallography Open Database". In: *Journal of Cheminformatics* 10.1 (May 2018). DOI: 10.1186/s13321-018-0279-6.

[19] A Merkys et al. "*COD::CIF::Parser*: an error-correcting CIF parser for the Perl language". In: *Journal of Applied Crystallography* 49.1 (Feb. 2016). DOI: 10.1107/S1600576715022396. URL: http://dx.doi.org/10.1107/S1600576715022396.

[20] S Gražulis et al. "Computing stoichiometric molecular composition from crystal structures". In: *Journal of Applied Crystallography* 48.1 (Feb. 2015), p. 85. DOI: 10.1107/S1600576714025904. URL: http://dx.doi.org/10.1107/S1600576714025904.

[21] S Gražulis et al. "Crystallography Open Database (COD): an open-access collection of crystal structures and platform for world-wide collaboration". In: *Nucleic Acids Research* 40.D1 (2012), p. D420. DOI: 10.1093/nar/gkr900. eprint: http://nar.oxfordjournals.org/content/40/D1/D420.full.pdf+html. URL: http://nar.oxfordjournals.org/content/40/D1/D420.abstract.

[22] S Gražulis et al. "Crystallography Open Database – an open-access collection of crystal structures". In: *Journal of Applied Crystallography* 42.4 (Aug. 2009), p. 726. DOI: 10.1107/S0021889809016690. URL: http://dx.doi.org/10.1107/S0021889809016690.

[23] RT Downs and M. Hall-Wallace. "The American Mineralogist Crystal Structure Database". In: *American Mineralogist* 88 (2003), p. 247.

[24] JM Moreau et al. "Ferroelectric $BiFeO_3$ X-ray and neutron diffraction study". In: *Journal of Physics and Chemistry of Solids* 32.6 (1971), p. 1315.

[25] P Suresh and S Srinath. "Observation of high coercivity in multiferroic lanthanum doped $BiFeO_3$". In: *Journal of alloys and compounds* 554 (2013), p. 271.

[26] M Nagl et al. "A new tool for the search of nuclides with properties suitable for nuclear solid state physics based on the Evaluated Nuclear Structure Data Files". In: *Nuclear Instruments and Methods in Physics Research Section A: Accelerators, Spectrometers, Detectors and Associated Equipment* 726 (2013), p. 17.

[27] A Jancso et al. "TDPAC and β-NMR applications in chemistry and biochemistry". In: *Journal of Physics G: Nuclear and Particle Physics* 44.6 (2017), p. 064003.

[28] JF Ziegler. *SRIM-2013 software package*. URL: http://www.srim.org.

[29] GS Arya, RK Kotnala, and NS Negi. "Structural and multiferroic properties of $Bi_{1-x}In_xFeO_3$ ($0\leq x\leq 0.20$) nanoparticles". In: *Journal of Applied Physics* 113.4 (2013), p. 044107.

[30] GS Arya and NS Negi. "Effect of In and Mn co-doping on structural, magnetic and dielectric properties of $BiFeO_3$ nanoparticles". In: *Journal of Physics D: Applied Physics* 46.9 (2013), p. 095004.

[31] J Gebhardt and Andrew M Rappe. "Doping of $BiFeO_3$: A comprehensive study on substitutional doping". In: *Physical Review B* 98.12 (2018), p. 125202.

[32] A Abragam and RV Pound. "Influence of electric and magnetic fields on angular correlations". In: *Physical Review* 92.4 (1953), p. 943.

[33] G Schatz and A Weidinger. "Nuclear condensed matter physics. Nuclear methods and applications". In: (1996).

[34] H Frauenfelder and RM Steffen. "Alpha-, Beta-, and Gamma-Ray Spectroscopy". In: *Angular Correlation* (1965), p. 997.

[35] EO Ayieta. "effects Of Absorbers on Perturbed Angular Correlation Spectrum". PhD thesis. Miami University, 2004.

[36] E Dafni et al. "Tables of SnNk1k2 and skn for γ-ray perturbed angular correlations with quadrupole interactions". In: *Atomic data and nuclear data tables* 23.4 (1979), p. 315.

[37] E Danielsen et al. "Structure of metal site in azurin, Met 121 mutants of azurin, and stellacyanin investigated by 111m CD perturbed angular correlation (PAC)". In: *Journal of Biological Chemistry* 270.2 (1995), p. 573.

[38] GN Darriba et al. "Experimental TDPAC and theoretical DFT study of structural, electronic, and hyperfine properties in (111In→) 111Cd-doped SnO2 semiconductor: ab initio modeling of the electron-capture-decay after-effects phenomenon". In: *The Journal of Physical Chemistry C* 122.30 (2018), p. 17423.

[39] J Schell, Peter Schaaf, and Doru C Lupascu. "Perturbed angular correlations at ISOLDE: A 40 years young technique". In: *AIP Advances* 7.10 (2017), p. 105017.

[40] K Lorenz. "Implantationsstudien an Gruppe-III-Nitriden". In: *Doctor thesis, University of Bonn* (2002).

[41] ME Rose. "The analysis of angular correlation and angular distribution data". In: *Physical Review* 91.3 (1953), p. 610.

[42] RS Hager and EC Seltzer. "Internal conversion tables part II: Directional and polarization particle parameters for Z= 30 to Z= 103". In: *Nuclear Data Sheets. Section A* 4.5-6 (1968), p. 397.

[43] M. Deicher (Universität des Saarlandes). Private communication. 2021.

[44] BL (Louisiana State University) Dutrow and CM (Eastern Michigan University) Clark. *X-ray Powder Diffraction (XRD).* Visited 2020. URL: `https://serc.carleton.edu/research_education/geochemsheets/techniques/XRD.html`.

[45] M Kaliva and M Vamvakaki. "Chapter 17 - Nanomaterials characterization". In: *Polymer Science and Nanotechnology*. Ed. by Ravin Narain. Elsevier, 2020, p. 401. ISBN: 978-0-12-816806-6. DOI: https://doi.org/10.1016/B978-0-12-816806-6.00017-0. URL: http://www.sciencedirect.com/science/article/pii/B9780128168066000170.

[46] Wikipedia. *Bragg's law*. Visited 2020. URL: https://en.wikipedia.org/wiki/Bragg%5C%27s_law.

[47] K Freitag. "A facility for ion implantation in samples colder than 0.5 k". In: *Radiation Effects* 44.1-4 (1979), p. 185.

[48] *The ISOLDE facility*. Visited 2020. URL: https://isolde.cern/isolde-facility.

[49] K Johnston et al. "The solid state physics programme at ISOLDE: recent developments and perspectives". In: *Journal of Physics G: Nuclear and Particle Physics* 44.10 (2017), p. 104001.

[50] J Schell et al. "Ion implantation in titanium dioxide thin films studied by perturbed angular correlations". In: *Journal of Applied Physics* 121.14 (2017), p. 145302.

[51] ML Arenz. *Production and PAC studies of $^{83}Rb/^{83m}Kr$ solid state calibration sources for the KATRIN experiment*. 2017.

[52] M Nagl et al. "A new all-digital time differential γ-γ angular correlation spectrometer". In: *Review of Scientific Instruments* 81.7 (2010), p. 073501.

[53] M Nagl. "Next-Generation Perturbed Angular Correlation Spectroscopy". In: (2014).

[54] J. G. M. Correia (CERN). Private communication. 2020.

[55] AML Lopes et al. *Local Probing Of Ferroic And Multiferroic Compounds*. Tech. rep. 2017.

[56] Hans Hofsäss. "Perturbed $\gamma - \gamma$ angular correlation. Program version 5.25." Jan. 20, 2002.

[57] T. Butz (Leipzig University). "TD-PAC Data Acquisition and Evaluation System. (C) JL 2000-2002. Version modified in 2009 by Daniel Silva and Joao Horta, Portugal".

[58] NP Barradas. *NNFit core program: PAC Manual*. Lisbon (1992).

[59] NP Barradas et al. "Magnetic anisotropy and temperature dependence of the hyperfine fields of Cd 111 in single-crystalline cobalt". In: *Physical Review B* 47.14 (1993), p. 8763.

[60] J. G. Correia. *GFit19 software. Available upon request to author: joao@cern.ch*. 2019.

[61] J Landers et al. "Mössbauer study of temperature-dependent cycloidal ordering in $BiFeO_3$ nanoparticles". In: *Nano letters* 14.11 (2014), p. 6061.

[62] J Schell et al. "Strong magnetoelectric coupling monitored at an atomic non-magnetic electro-magnetometer in bismuth ferrite". Submitted to the PRB in 2020.

[63] ME Lines and Alastair M Glass. *Principles and applications of ferroelectrics and related materials*. Oxford university press, 2001.

[64] Wikipedia. *Landau Theory*. URL: https://en.wikipedia.org/wiki/Landau_theory.

[65] M Forker. "The problematic of the derivation of the electric fieldgradient asymmetry parameter from TDPAC measurements or Mössbauer spectroscopy in imperfect crystal lattices". In: *Nuclear Instruments and Methods* 106.1 (1973), p. 121.

[66] Malvern Panalytical. *HighScore XRD Analysis Software*. URL: `https://www.malvernpanalytical.com/en/products/category/software/x-ray-diffraction-software/highscore`.

Appendix A

Additional figures and tables

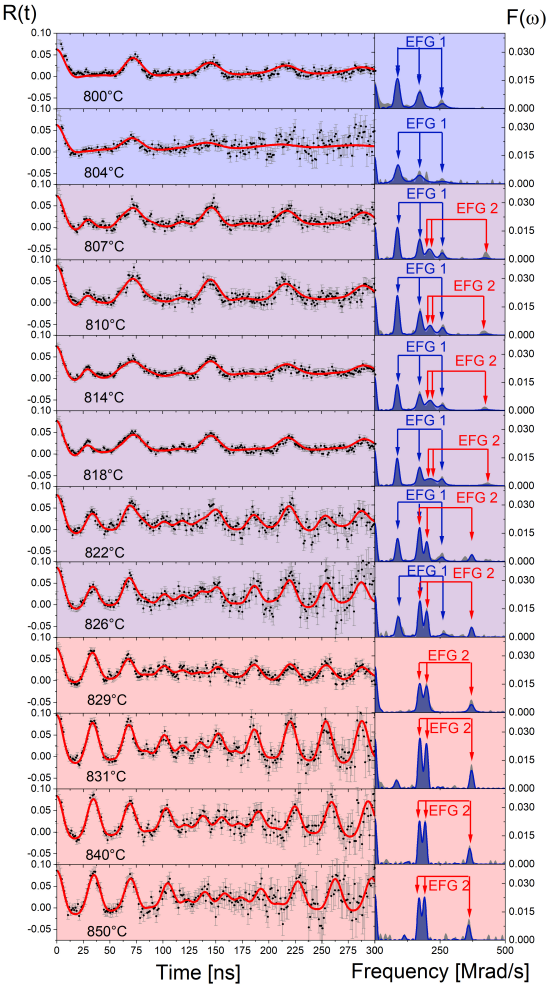

Figure A.1: Energy spectra R(t) and FFT of research with BFO(^{111m}Cd). Taken from literature G. Marschick et al. "Multiferroic bismuth ferrite: Perturbed angular correlation studies on its ferroic $\alpha - \beta$ phase transition". In: Phys. Rev. B 102, 224110 – Published 29 December 2020.

	α-phase	α-phase			β-phase			
Temp [°	%	ω_0 [Mrad/s]	η [1]	δ [%]	%	ω_0 [Mrad/s]	η [1]	δ [%]
370	100(0)	130(8)	0.02(0)	0.25(1)				
380	100(0)	129.83(11)	0(4)	0.24(2)				
400	100(0)	128.88(7)	0.061(0)	0.034(1)				
450	100(0)	126.87(16)	0.07(1)	0.355(9)				
500	100(0)	126.82(16)	0.07(0)	0.363(10)				
600	100(0)	119.7(13)	0.028(1)	0.686(10)				
650	100(0)	115.72(27)	0(1)	1.502(6)				
700	100(0)	112.67(18)	0(2)	0.991(5)				
750	100(0)	107.34(20)	0(2)	1.25(5)				
800	100(0)	102.43(14)	0(1)	0.664(4)				
807	100(0)	101.37(15)	0(2)	0.773(4)				
810	100(0)	101.03(19)	0(3)	0.872(3)				
814	100(0)	100.28(15)	0.04(0)	0.83(5)				
818	100(0)	100.14(14)	0(2)	0.639(3)				
822	100(0)	99.48(13)	0.03(0)	0.49(4)				
829	100(0)	98.16(18)	0.105(0)	0.441(4)				
835					100(0)	19.9(20)	0.63(1)	2.53(69)

Table A.1: KATAME hyperfine parameter vales and their estimated uncertainties as obtained by the analysis software[58],[59],[60].

	α-phase				β-phase			
Temp. [°]	%	ω_0 [Mrad/s]	η [1]	δ [%]	%	ω_0 [Mrad/s]	η [1]	δ [%]
370	100(0)	129.78(16)	0(0)	0(0)				
380	100(0)	129.6(21)	0(0)	0(0)				
400	100(0)	128.55(10)	0(2)	0.51(21.4)				
550	100(0)	121.88(17)	0(5.7)	0.291(13.4)				
600	100(0)	119.05(20)	0(8)	0(13)				
649	100(0)	114.59(24)	0.1(0)	1.615(34)				
700	100(0)	111.28(16)	0(2)	0(97)				
750	100(0)	106.83(19)	0(0)	0.044(19)				
800	100(0)	100.25(15)	0(1)	0.23(1)				
807	100(0)	100.22(13)	0(3)	0(89)				
810	100(0)	99.87(14)	0(4)	0.054(4)				
814	100(0)	99.75(16)	0(3)	0.052(5)				
818	100(0)	99.05(17)	0.02(5)	0.029(6)				
822	100(0)	98.54(14)	0(0)	0.057(5)				
829					100(0)	22.13(14)	0.772(1)	2.831(20)
835					100(0)	23.86(11)	0.474(1)	0.598(21)
840					100(0)	20.47(11)	0.862(1)	10.941(57)

Table A.2: K1 hyperfine parameter values and their estimated uncertainties as obtained by the analysis software[58],[59],[60].

System		$V_{zz}^{DFT}[\frac{10^{21}V}{m^2}]$	η^{DFT} [1]	ΔH^{DFT} [eV]	ω_0^{DFT} [Mrad/s]
α-BFO (FM / AFM)	Cd @ Bi	5.72 / 5.37	0/0	8.4 / 2.6	80.3-86.8 / 75.4-81.5
	Cd @ Fe	5.46 / 4.07	0/0	8.8 / 5.5	76.7-82.9 / 57.1-61.8
β-BFO (FM / AFM)	Cd @ Bi	-7.51 / -6.88	0.39 / 0.26	4.2 / 1	105.4 - 113.97 / 96.57 - 104.41
	Cd @ Fe	2.37 / 8.43	0.87 / 0.18	5.4 / 2.2	33.3 - 35.9 / 118.33 - 127.93
$Bi_2Fe_4O_9$ (FM)	Cd @ Bi	9.99	0.12	-	140.22 - 151.61
	Cd @ Fe	7.99	0.84	-	112.15 - 121.25

Figure A.2: DFT simulations made for research with BFO(^{111m}Cd). Taken from literature G. Marschick et al. "Multiferroic bismuth ferrite: Perturbed angular correlation studies on its ferroic $\alpha - \beta$ phase transition". In: Phys. Rev. B 102, 224110 – Published 29 December 2020.

Appendix B

Detailed calculations

B.1 Electric field gradient (EFG)

Derivation taken from [2].

It is defined as the traceless component of the second spacial derivative of the electrostatic potential:

$$V_{ij} = \frac{\partial^2 V}{\partial x_i^2 \partial y_j^2}$$

It is a 3x3 tensor, which can be diagonalized through a coordination transformation into the diagonal elements V_{xx}, V_{yy}, V_{zz}. the reference system is set such so the largest component points in the z-direction: $|V_{zz}| \geqslant |V_{yy}| \geqslant |V_{xx}|$

Using the Laplace equation: $V_{zz} + V_{yy} + V_{xx} = 0$, the EFg can be described by only two parameters, the largest component of the tensor, V_{zz}, and the asymmetry parameter, η:

$$\eta = \frac{V_{xx} - V_{yy}}{V_{zz}}$$